STAR-SHAPED BUBBLES AND CUBIC FECES: GEOMETRY THROUGH SOFT MATTER

A Dissertation
Presented to
The Academic Faculty

By

Alexander Bo-Ping Lee

In Partial Fulfillment
of the Requirements for the Degree
Doctor of Philosophy in the
School of Biological Sciences
Quantitative Biosciences

Georgia Institute of Technology

December 2020

STAR-SHAPED BUBBLES AND CUBIC FECES: GEOMETRY THROUGH SOFT MATTER

Thesis committee:

Dr. David Hu, Advisor
Schools of Mechanical Engineering and Biological Sciences
Georgia Institute of Technology

Dr. Donald Webster
School of Civil and Environmental Engineering
Georgia Institute of Technology

Dr. Julia Kubanek
School of Biological Sciences
Georgia Institute of Technology

Dr. Peng Qiu
School of Biomedical Engineering
Georgia Institute of Technology

Dr. Alexander Alexeev
School of Mechanical Engineering
Georgia Institute of Technology

Date approved: November 10th, 2020

To the many teachers who have supported me and changed my life for the better.

And to my wife and family. Thank you for all of your love and support,

and telling me to get back to work when I got distracted.

ACKNOWLEDGMENTS

TABLE OF CONTENTS

SUMMARY

In this thesis, we consider how mammals use soft tissue to generate geometric shapes out of non-living materials. The star-nosed mole sniffs for prey underwater by rapidly exhaling and inhaling bubbles without letting the bubbles pinch off. The bare-nosed wombat forms cubic feces, displaying 6 flat sides and 8 rounded corners. We develop mathematical models supported by simple table-top experiments to better understand how these mammals accomplish such amazing feats. These species control the fluids through interactions with solid tissue. Understanding these interactions could lead to innovations in chemical sensing and manufacturing.

CHAPTER 1

INTRODUCTION

In this thesis, we consider three cases studies of how shape influences physics, and vice versa. Since D'Arcy Thompson's "On Growth and Form" in 1942, biologists have known that much of the complexity and array of shapes in biology are made possible by physical interactions and signal between cells [1]. In this thesis, we focus on the surprising abilities of soft structures such as a mole's star nose or a wombat's intestines, can mold soft external materials into shapes that are useful for the animal.

Specifically, Chapter 2 looks at the star-nosed mole, whose namesake comes from the unique shape formed by the appendages sprouting from its nostrils. We study how the shape of the nose provides increased stability for their underwater bubble-sniffing (See **Figure 1.1e**). In chapter 3 we consider the bare-nosed wombat and how its intestines mold corners into its feces, resulting in its unique cubic feces (See **Figure 1.1f**). Chapter 4 looks at how drying breaks up feces in the intestines. This gets at how the axial length of the wombat's cubic feces are set, but also considers the comparative question of why some mammals have long cylindrical feces (**Figure 1.1h**), while others have pelleted feces (**Figure 1.1g**). We conclude in chapter 5 with some implications and directions for future work.

Throughout this thesis, we take a quantitative approach, calculating the forces that are applied to the external objects. Often times, the systems such as a wombat intestine are quite complex. They are three-dimensional, involving fluid-solid interactions non-Newtonian fluids and nonlinear materials for which there are no clear constitutive laws and governing equations. In those cases, we take necessary simplifications into two dimensions and simplifying fluid dynamics into simple springs and dampers. We ground our modeling through the use of dimensionless numbers to relate competition between relevant

forces. In Chapter 2, we use the Bond number to analyze the balance between the bubble's buoyancy and surface tension. Chapter 3 considers the balance between inertial and viscous effects with the Reynolds number. The Péclet number describes the competition between convection and diffusion in the motion of water during drying as we will discuss in Chapter 4.

Although the techniques used in this thesis are physics-based, the questions considered are relevant to evolutionary biology. One of the dominant themes in this thesis is that of form and function [2]. One of the classic illustrating examples is of Darwin's finches in which the beak shape between species allows them to occupy different ecological niches [3]. Wide beaks might be better adapted to eat fruit, while small slender beaks are better at picking up insects (See **Figure 1.1a**). From molecular to ecological lengthscales, we understand that an object's dimensions and geometry characterize how that object interacts with the environment around it.

While it is important to keep in mind the paradigm of form and function, we must also be careful to not assume relationships between form and function prematurely. In doing so, we risk prescribing purpose to geometries that are the side-effect of other phenomenon [4].

Throughout this thesis, we will be considering the patterns formed in excrement and other non-living materials that are formed by the animal. Animals are long known to do molding of external objects in a range of circumstances. A prominent example is he elaborate homes of social insects, from termites to repeated hexagonal combs of bee hives [5] are formed by the collective sculpting actions from the group. The intestines we will consider in Chapter 3 also act like sculptors in that multiple contractions and specialized material properties enable the final shape. Its no accident that social insects form malleable materials such as mud and beeswax, and that the animals in our study make patterns in feces. The forces applied by animals are sufficiently low that the materials should be soft enough to be deformed.

Another dominant theme in this thesis is the formation of shape due to the principle of

minimization of energy. A system's attraction towards states of minimum energy plays an implicit role in stabilizing bubbles as discussed in Chapter 2. In our everyday lives, we see shape minimization at work in drops and bubbles, whose shapes are governed by capillarity, the physics of fluid interfaces. Drops and bubbles are more closely resembling spheres at small enough lengthscales: here, body forces such as gravity become less dominant, and capillary or surface forces become more dominant. Capillary forces are a result of the affinity that molecules have for similar molecules, most notable is the affinity that water molecules have for other, hydrophilic, water molecules [6].

However, at larger scales, these capillary forces compete with other forces, leading to shapes that differ from sections of spheres. Sufficiently large pendent drops and bubbles are stretched out of their spherical shape by gravity, forming elongated necks (See **Figure 1.1d**). The contour of the neck determines the size and rate at which the drop pinches off from the faucet, or the bubble pinches off from a nozzle [7, 8, 9, 10]. This physical picture has led to the study of different nozzle geometries to get the most frequent, smallest bubbles in aquarium bubblers and metallurgical industrial processes [11, 12, 13, 14, 15]. When a central stream of water strikes a kitchen sink, a roughly circular standing wave of fluid is created, known as a hydraulic jump. When the fluid is viscous, interface minimization is lost as corners form in the hydraulic jump, taking the shape of a polygon (See **Figure 1.1b**) [16, 17]. Star-nosed moles blow bubbles to detect odors underwater [18]. These bubbles deform as they are blown against surfaces that carry the odors of their prey.

A bubble's size affects the forces dominating its shape. The size of a bubble determines its resonant frequency, strongly influencing its mass transfer rates in an oscillatory environment [19]. The size not only affects the magnitude of forces acting on it: its buoyancy, surface tension, and drag, but also its added mass, the amount of fluid that must be displaced for it to move, distinctly affecting the bubble's kinematics [20]. The work required to alter the contact angles formed between drops and bubbles against inclined solids can pin them in place against gravity [21, 22, 23]. Similarly, in Chapter 2 we will see that the
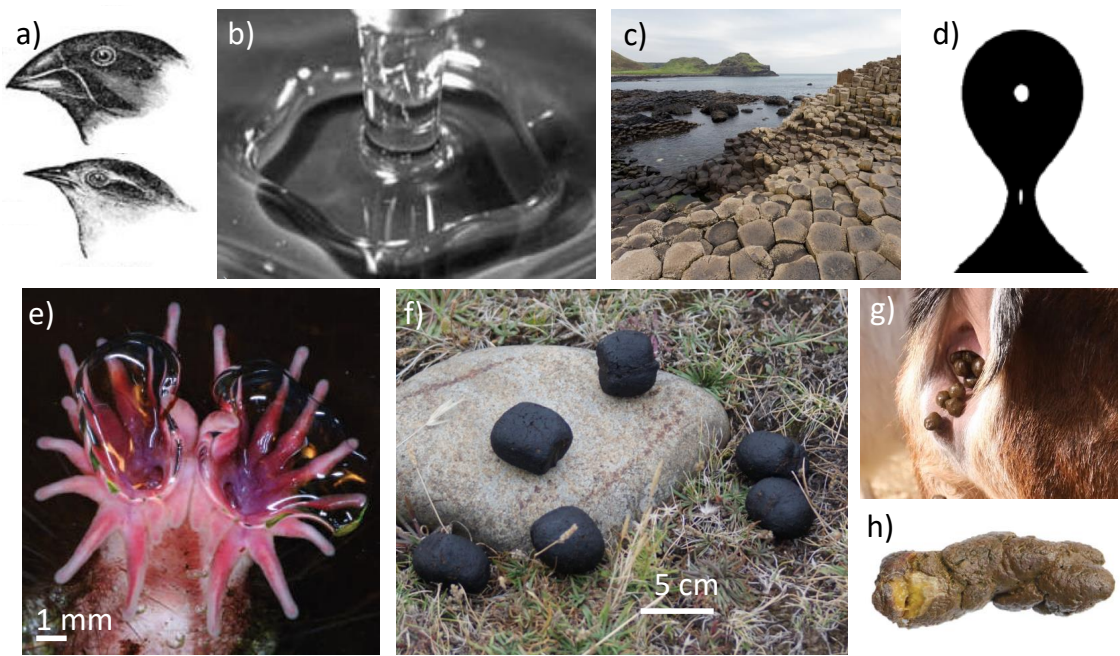
Figure 1.1: Shapes in nature. (a) Beaks of Darwin's finches (https://en.wikipedia.org/wiki/Darwin%27s_finches). (b) Polygonal hydraulic jumps. (c) Columnar jointing at Giant's Causeway (https://electricbluefood.com/giants-causeway-autumn-morning/). (d) Pinch-off of a pendant bubble. (e) The nose of the star-nosed mole. (f) The bare-nosed wombat's cubic feces. (g) Goats' pelleted feces versus dogs' cylindrical feces.

shapes that the star-nosed mole forces the bubble into can alter the bubble's stability.

Outside of fluid dynamics, many physical processes give rise to geometric patterns. The processes of cooling lava at Giant's Causeway Ireland leads to hexagonal columns called columnar jointings (See **Figure 1.1c**) [24]. They are created by regular cracking patterns that occur everywhere from cornstarch slurries drying in a lab to dried out lake beds found on the surface of Mars [25]. We will also look at various mammals in Chapter 4 that are capable of breaking up their feces at regular intervals to form pellets.

CHAPTER 2

BUBBLE-STABILIZATION BY THE STAR-NOSED MOLE

2.1 Introduction

We begin this thesis with an investigation of the unique geometry of the star-nosed mole, which it uses to alter the shape of the bubbles that it blows from its nostrils. We consider how the altered bubble shape stabilizes the bubble, keeping it centered upon the star-nosed mole's nostril, allowing the bubble to be sucked up again, rather than pinch-off.

The bubbles of the star nosed mole acts as an underwater chemical sensor. In general, chemical sensors are not amphibious: they are deployed in either a liquid or gas phase, but not both [26]. The same limitation holds for our noses. We cannot smell underwater, and it was once believed that aquatic mammals also had a poor sense of smell underwater [18]. A number of small semi-aquatic mammals, however, have evolved ingenious ways to adapt their noses to locate food underwater.

Smelling underwater begins with an exhale of a bubble. When the bubbles contacts a food item, it gathers odorant molecules, which otherwise would not make their way past the air-water barrier in the animal's nose. The bubble is then inhaled before it has a chance to pinch off and escape. **Figure 2.1** shows the star-nosed mole (*Condylura cristata*), the American water shrew (*Sorex palustris*) [27], and the Russian desman (*Desmata moschata*) [28], all of which sniff bubbles on a timescale of 0.07 - 0.1 seconds. The inhalation flow rates of these semi-aquatic mammals range from 0.7 - 2 mL/s, approximately twice as fast as same-sized terrestrial counterparts [29].

From hereon, we will focus our attention on the star-nosed mole, the most documented of these underwater sniffers (See **Figure 2.2a**). The mole's behavior allows the odor receptors in it's nose to stay dry, relying on the bubble's rapidly generated surface area as a

6
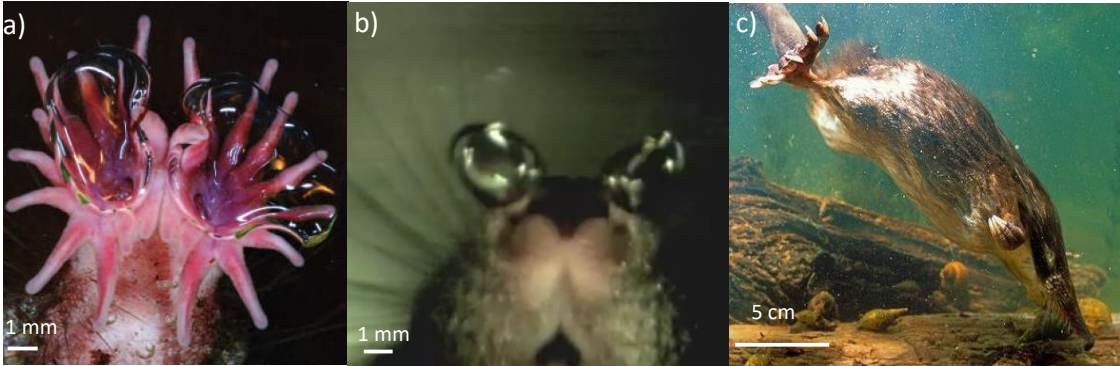
Figure 2.1: Three semi-aquatic mammals exhibit underwater sniffing: (a) the star-nosed mole blows a bubble of 0.1 mL on a timescale of 0.1 seconds, (b) the American water shrew blows a bubble of 0.06 mL on a timescale of 0.08 seconds, and (c) the Russian desman blows a bubble of 0.3 mL on a timescale of 0.07 seconds. Photographs (a,b) courtesy of K. Catania. Photograph (c) courtesy of I. Shpilenok.

medium to transport odor. Imitating this underwater sniffing would be an important first step towards employing gas sensors in aquatic environments. However, little is known about how to stabilize underwater bubbles larger than the capillary length, the length scale at which bubbles generally pinch off. Below we review how bubbles pinch-off and are stabilized by rough surfaces.

Bubble pinch-off has been studied in a number of contexts. As the neck of a bubble shrinks below some critical length scale [9][30], capillary forces irreversibly drive pinch-off, often quite quickly. In bubble formation from a downward nozzle, centimeter-scale bubbles, similar in size to that generated by the star-nosed mole, can pinch off in time-scales of 76 ms [11], three times as fast as the blink of an eye.

One way to delay pinch-off is to use rough substrates to stabilize the bubble. Micro-scopic surface roughness known as asperities can grab hold of a bubble's edge, called its contact line, leading to the bubble exhibiting a range of contact angles, a phenomenon called contact angle hysteresis. This hysteresis can hold drops and bubbles in place, even on vertical surfaces [21, 22, 31, 32]. This phenomenon can only pin drops on the size of

the capillary length, an equivalent volume of a few microliters, orders of magnitude smaller than the 0.1 mL volume of the star-nosed mole bubble[18].

Larger bubbles can be trapped by increasing the surface roughness to the extent that it obtains a Cassie-Baxter state, which makes it energetically unfavorable to displace the bubble and wet the surface [33]. Diving beetles and spiders employ densely packed hydrophobic hair to carry bubbles with them so they can breathe underwater [34, 35]. Their rough, hydrophobic surfaces are energetically costly to wet, allowing the maintenance of an air bubble of up to 3 mL in volume [36, 33, 35]. While it is possible that the microscopic surface features of the star-nosed mole may help retain bubbles, we will focus on its macroscopic features.

In this study, we investigate the mechanism by which the star-nosed mole stabilizes its exhaled bubbles. We begin in §2 with the results of experimental work in stabilizing bubbles against plastic stars mimicking that of the star-nosed mole. We discuss the implications of our work in §3 and conclude in §4. We our experimental methods for building and testing plastic stars that mimic that of the star-nosed mole. In §5, we present our detailed methods.

2.2   Results

Videos of star-nosed moles sniffing[27] show that when the star-nosed mole sniffs underwater, it often tilts its head from side to side. The driving idea behind this study is that the shape of the star helps stabilize the bubble while it is tilted.

2.2.1   Measuring the star-nosed mole

We obtain three photographs of live star-nosed moles from the author of a previous study [37]. The star-nosed mole has 22 conical fleshy appendages radiating from two nostrils, as shown in **Figure 2.2a**. To characterize the spacing between these appendages, we measure the gap angle, or the angle between the edges of two consecutive appendages, as illustrated in **Figure 2.2b**. The outermost section is chosen so that the gap angle accurately describes

the width of the gap where the spacing is widest. The wider the gap, the more likely buoyancy can begin to dominate over surface tension forces. In **Figure 2.2b**, appendages 9 and 10 are an example of overlapping appendages and are not considered in our measurements.
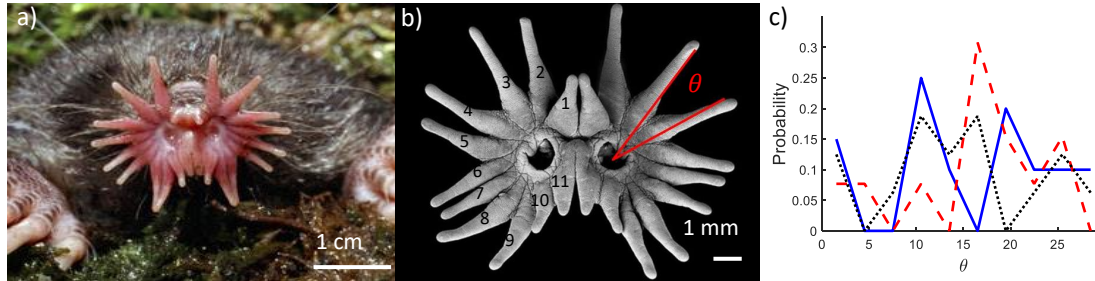
Figure 2.2: Geometry of the nose of the star-nosed mole. (a) The star-nosed mole, whose fleshy, star-shaped nose measures approximately 10 mm across. (b) Close up photograph of the nose, with red lines showing how the gap angle θ is measured. The red line is drawn between the center of the nostril and the inside tip of the appendages. (c) Histogram showing the distribution of the gap angles θ for three star-nosed moles. Photograph (a) and (b) courtesy of K. Catania.

Figure 2.2c shows a histogram of the gap angles from the three star-nosed mole photos. The histogram does not show a normal distribution, but is instead bimodal due to the ventral parts of the star having more closely spaced arms. This may have to do with the mechano-sensing role that these lower appendages play [37]. The average gap angle is $16\pm9°$ (N = 49 arms counted on 3 moles). Due to the large standard deviation, we conclude that the arms are of order $10°$ apart, a number which we try to rationalize using experiments with our plastic stars.

2.2.2   Bubble stability experiments

Plastic stars are designed in Solidworks. We begin with a circular disk with a central hole for the nozzle. Around the hold, a ring of solid plastic forms the center of the star. Triangular arms are cut extending from this ring by making radial cuts that form gaps, characterized in size by the gap angle θ used to characterize the nose of the star-nosed mole.

With the star submerged in water, we use a syringe to inflate a sessile bubble of $V_t = 0.7$ mL beneath the plastic star. As a test of the bubble's stability, we slowly tilt the syringe until we discover the angle ϕ to the vertical at which the bubble pinches off (See **Figure 2.3a**). **Figure 2.3b** shows the relationship between the gap angle θ and the maximum tilt angle before pinch-off ϕ. Among our five stars, the $8°$ and $15°$ stars exhibit the highest stability, holding the bubble until they are tilted to nearly $8°$. This is about 150 percent higher than the lowest performing star, the $20°$ star. Moreover, the arms are clearly useful in holding onto the bubble. The best performing stars can hold onto bubbles at angles that are almost twice as large as a flat plate.

We first consider the dimensionless Bond number of our system, which relates the buoyancy to surface tension forces. The Bond number may be written

$$Bo = \frac{\Delta \rho g D_{eq}^2}{\sigma} \tag{2.1}$$

where $\Delta \rho$ is the difference in density between the water and air, g is the gravitational acceleration, σ is the interfacial surface tension between water and air, and $D_{eq} = \left(\frac{6V_t}{\pi}\right)^{1/3}$ is the equivalent spherical diameter of a bubble of volume V_t [38]. For bubbles of volume $V_t = 0.7$ mL, the Bond number is 16, suggesting that buoyancy forces are dominant. This number also indicates that the bubble is highly unstable. This is ultimately why bubbles can only be tilted to less than $\phi_c = 10$ degrees before they escape. If we consider gravity in our tilting system to be $g \sin \phi_c$, then the Bond number is 3, showing that the tilt angle of $\phi_c = 10°$ marks the transition between surface tension-dominated to buoyancy-dominated regimes. The Bond number is greater than 1, suggesting that the bubbles should be released. We proceed by presenting theory on how this buoyancy-dominated system could remain stable.
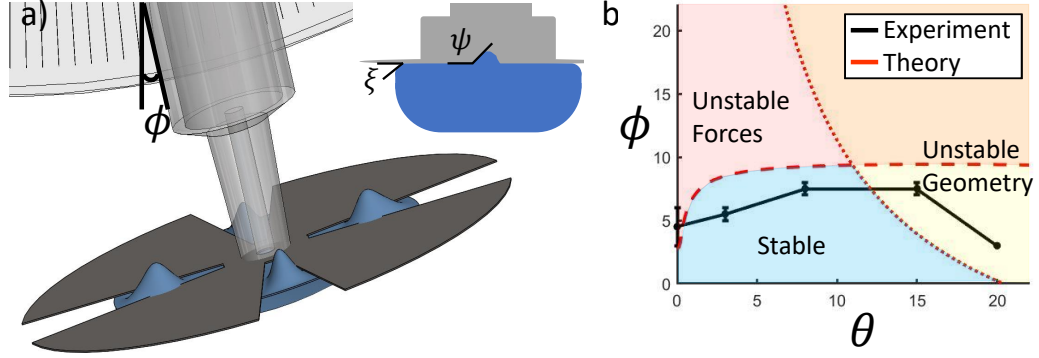
Figure 2.3: (a) Schematic of the experimental setup in which a syringe with a plastic star is affixed to a protractor. As a measure of bubble stability, the syringe is tilted at an angle ϕ before the bubble pinches off. Inset shows the contact angle, $\xi = 54°$, of the bubble below the star and the angle, $\psi = 127°$, of the bubble pushing up through the gap. (b)The relationship between the maximum tilt angle ϕ and the gap angle θ of the star. Experimental data (black) suggests an optimal gap angle around $8° - 15°$, and the theory predicts an optimum at $11° \pm 3°$. The theory described in §3 describes a large gap condition leading to pinch-off (red dotted line) and a small gap condition leading to pinch-off (red dashed line).

2.2.3   Theory

Our theory predicts pinch-off to occur when one of two conditions is broken. We consider each condition in turn.

For large gap angles, pinch-off occurs when buoyancy forces dominate capillary forces. This occurs when the width of the gap is greater than the capillary length [6], $\lambda_c = \sqrt{\frac{\sigma}{\Delta \rho g}}$ where σ is the surface tension between two fluids, $\Delta \rho$ is the difference in density between the two fluids, and g is the acceleration due to gravity. For air bubbles in water, the capillary length is $\lambda_c = 2.7$ mm. Thus, if a region of the bubble is exposed to a gap width larger than λ_c, the bubble will escape.

Considering the advancing side first, the bubble radius may be written as the central plastic disc radius R plus some incremental distance, ΔR_a, as shown in **Figure 2.4d**. By etching 1 mm markings on the edges of the star, we measure the motion of the bubble's contact lines for different tilt angles, ϕ, using a star with gap angles of $\theta = 8°$ as that is the median gap angle. The red points in **Figure 2.4e** show the change in radius of the

advancing side of the bubble, ΔR_a, as a function of tilt angle. The associated changes, ΔR_r on the receding side of the bubble are shown in blue triangles. The blue and red lines show the linear least squares best fit, which are

$$\Delta R_a = \alpha + \beta\phi \ (R^2 = 0.5) \tag{2.2}$$

for the advancing side, and

$$\Delta R_r = \alpha - \gamma\phi \ (R^2 = 0.3). \tag{2.3}$$

for the receding side, where ΔR_a and ΔR_r are given in mm, ϕ in degrees, and $\alpha = 4$ mm, $\beta = 0.7\frac{mm}{degree}$, and $\gamma = 0.3\frac{mm}{degree}$. The non-equality of the slopes β and γ indicate that the bubble is not just sliding but also deforming. Specifically, the bubble is stretching as it rises. Visually, the fits given in **Equation 2.2** and **Equation 2.3** follow the data well, as shown in **Figure 2.4e**. The goodness of fit R^2 values are low, due to data standard deviation being large relative to β and γ,as the R^2 value is a metric of how much better the linear regression is as a predictor than a horizontal line at the data's mean. More importantly, the Root Mean Squared Error (RMSE) is 1 mm for both the advancing and receding regressions. The trends from our theory are not significantly changed by this magnitude of error. By considering how the advancing side displaces as the system is tilted, we may predict the tilt angle ϕ at which the bubble pinches off as a function of the gap angle θ (See **Figure 2.3b**, red short dashed line).

As the bubble is tilted further, it encounters an increasingly wider gap at the advancing side, as shown in **Figure 2.5a**. The blue hashed region indicates the bubble, which intersects the two consecutive arms of the star holding it in place. At this intersection, the arms are separated by a gap width $2(R + \Delta R_a)\tan\frac{\theta}{2}$. The bubble is stable as long as this gap

width is less than the capillary length:

$$2(R + \Delta R_a) \tan \frac{\theta}{2} \leq \epsilon \lambda_c \tag{2.4}$$

where ϵ is a numerical prefactor, that accounts for the bubbles pinching off at length scales directly correlated to the capillary length, as is the case in a number of context [39, 40]. Preliminary experiments, expanding bubbles under horizontal stars, with gap angles of $\theta = 3°$, $8°$, $15°$, and $20°$, indicate that the prefactor $\epsilon \approx 1$. Thus from hereon ϵ will be omitted from equations. Applying our empirical measurements of ΔR_a in **Equation 2.2**, we rewrite **Equation 2.4** relating ϕ to θ and solve for ϕ.

$$\phi \leq \frac{1}{\beta} \left(\frac{\lambda_c}{2 \tan \frac{\theta}{2}} - R - \alpha \right) \tag{2.5}$$

This equation can be used to predict the maximum ϕ with respect to θ (dotted red curve, **Figure 2.3b**). This shows agreement with our experimental data when the gap angle θ is $15°$ and $20°$, shown on the right hand side of **Figure 2.3b**. This concludes our analysis of stars of large gap angles; we now turn to stars of small gap angles. We begin with an an illustrative but more intuitive problem. Consider a weight sliding down a ramp with no friction. When the ramp is flat, no counterweight is needed. However, with any level of inclination, a counterweight is needed for equilibrium, as shown in **Figure 2.5c**. The same physics holds for the bubble trapped underneath a tilted star. Instead of gravitational force, two buoyancy forces act to pull the bubble in opposite directions. One force, $\rho g V \sin \phi$, is oriented parallel to the arms of the star, where V is the volume of the bubble in the red hashed region on the right of **Figure 2.4d** and **Figure 2.5b**. The other force, $\rho g v$, arises due to the bubble attempting to rise through the gaps on the receding side of the star. Thus, we take v to be the entire section of the bubble denoted by the blue hashed region on the
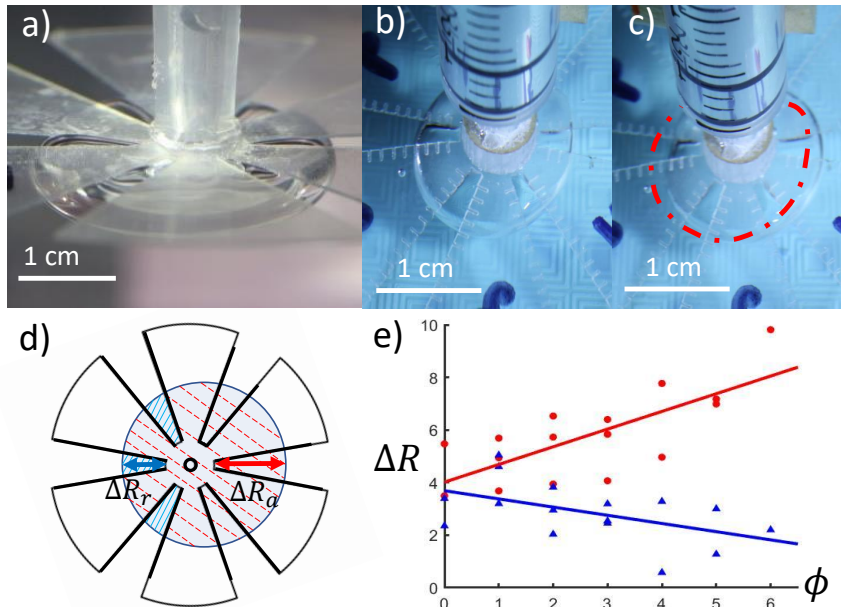
Figure 2.4: Position of the bubble with varying tilt angle ϕ. (a) Photograph shows portions of a bubble rising through the gaps between the arms of the star, forming ribs similar to a pumpkin. (bc) Two photographs showing the position of the bubble before and after the star is tilted by an angle of $4°$. The red dotted line shows the original position of the bubble. As the system is tilted, one side of the bubble advances, and the other recedes. (d) The shift in bubble position creates two lengths from the start of the gap to the edge of the bubble, ΔR_a and ΔR_r for the advancing and receding sides respectively. (e) The relationship between the the tilt angle ϕ and the position ΔR of the bubbles edge for a star of gap angle $\theta = 8°$. The advancing edge is shown as red dots, the receding edge as blue triangles. The solid lines are linear best fits. The bubble pinches off when the tilt angle $\phi = 8°$.

left of **Figure 2.4d** and **Figure 2.5b**. For these forces to balance, we require

$$\rho g V \sin \phi \leq \rho g v. \tag{2.6}$$

The calculations for V and v as a function of both the gap angle θ and the tilt angle ϕ are provided in detail in the Methods section. This equation is used to predict the maximum ϕ with respect to θ (dotted red curve, **Figure 2.3b**). This shows agreement with our experimental data when the gap angle θ is less that $15°$, shown on the left hand side of **Figure 2.3b**.

2.2.4 Counterbalance Experiment

To demonstrate the importance of counterbalance, we perform a stability tilting experiment with a bent disc. The bend at an angle of $\zeta = 15°$ allows part of the bubble to peek over the receding slope as shown in **Figure 2.6**. As a result, the disc can be tilted up to $\phi = 10°$, which is more than double the values found for the flat disc. Moreover, both discs are made of the same material, indicating that differences in geometry can make a big difference in the stability of the bubble (**Figure 2.7**). If we assume equal volume of bubble on both the receding and advancing slopes of the plastic, then we maintain equilibrium under the following condition (See **Figure 2.6b**)

$$\sin(\phi) = \sin(\zeta - \phi). \tag{2.7}$$

Solving for ϕ, we find that the system can tilt $8°$. This is comparable to the maximum tilt angle of $10°$ found in our experiment.

2.3 Discussion

In static tilting experiments, we showed how a star-geometry surface can add stability to a sessile bubble and that there is an optimal gap size, represented by the gap angle θ, that
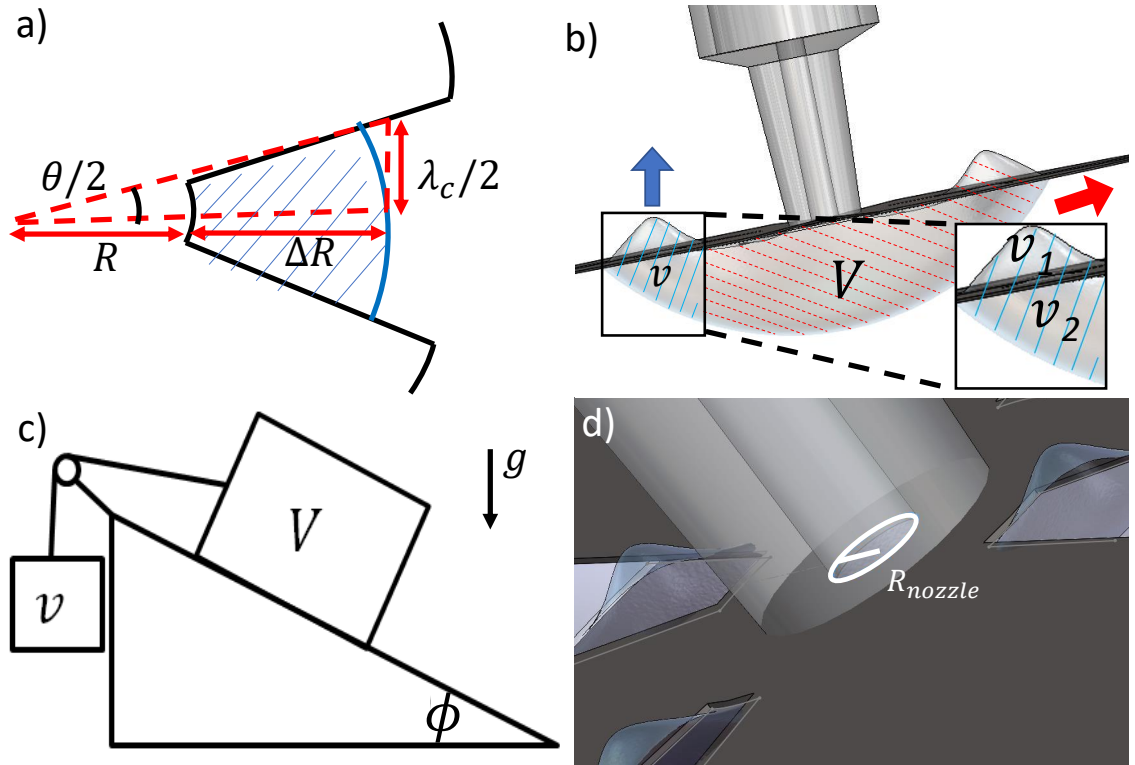
Figure 2.5: Illustrations of conditions preventing pinch-off. (a) Schematic of the gap and geometric pinch-off condition for large gap angles. (b) Side view schematics of the bubble interacting with the star shape above it. The buoyancy forces acting on the red region denoted by V are balanced by the buoyancy forces of the blue region of the bubble-star system for small gap angles. The portion of the bubble V (dashed red hashed region) slides off the star while the small portion in the gap, v (solid blue hashed region), acts as a counterbalance, similar to an analogous mass-on-a-ramp system shown in (c). Inset in (b) shows how v is split up into two regions v_1 and v_2 for volume calculations. (d) The parallel buoyant force must overcome the resisting surface tension force between the main bubble and air remaining in the syringe nozzle. Here, the radius R_{nozzle} is labeled.
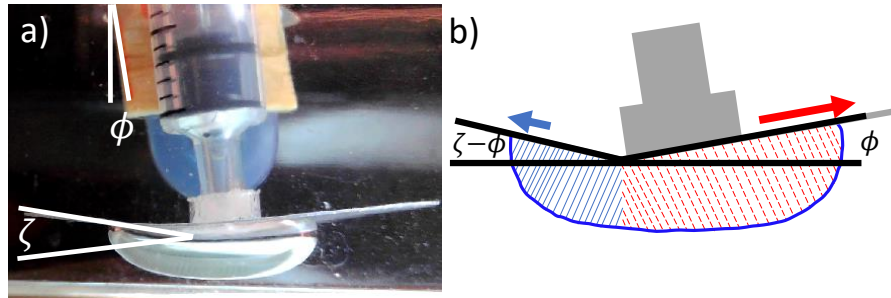
Figure 2.6: Schematic diagrams of the geometry of a bent plastic disc. (a) Photograph of the bubble held by the bent star and (b) schematic of the portions of the bubble showing counterbalance. The buoyancy force on the red hashed region causes the bubble to slide to the right. The bubble is held in place by the opposing buoyancy force on the blue hashed region.

$\phi = 3°$ $\phi = 5°$ $\phi = 7°$
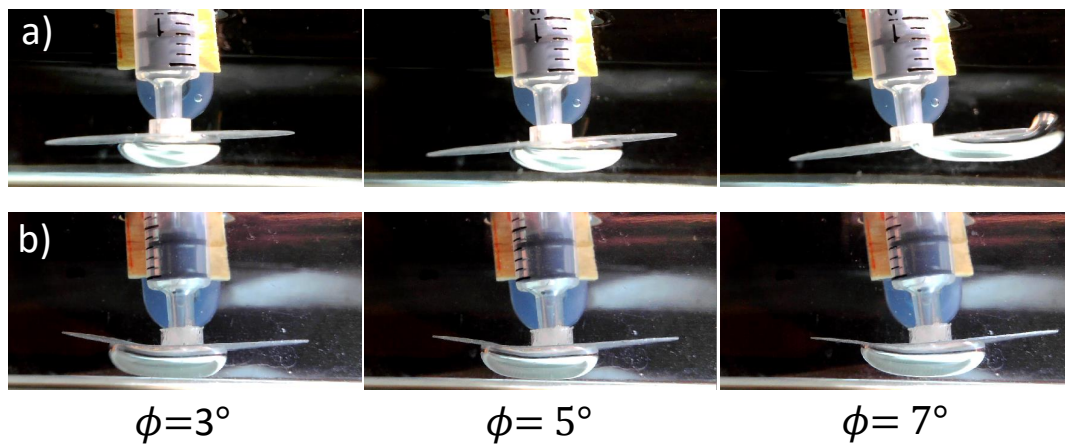
Figure 2.7: Experiments demonstrating the ability of a bubble to maintain counterbalance to remain stable. (a) A flat disc can only be tilted to $\phi = 4.5° \pm 1.5°$ before the bubble escapes. (b) A disc with a $\zeta = 15°$ bend at a position off-center can hold onto a bubble up to $\phi = 10°$ of tilt, demonstrating the importance of geometry in maintaining bubbles.

allows the sessile bubble to be stable at a higher tilting angle ϕ. Bubbles can slip through large gaps when the gap width is greater than the capillary length. Bubbles also fall out of static equilibrium when the gap is too small, due to the smaller counterweight effect from the bubble in receding side gaps.

The size of the gaps between the appendages in the mole's star-nose vary greatly with an average gap angle of $16°$. However, the distribution of gap angles show that most of the gap angles from the photos were either much lower or much higher than this value. When comparing the optimal physics to that of the biological system, it is important to keep in mind that these appendages also have a role in tactile sensing. The roles of tactile sensing and bubble stability encompassed in the same organ can lead to evolutionary trade-off and it would be a mistake to assume that a given organ would necessarily be optimized to any one role [4].

While this study set out to show the role of the mole's star-nose, our experiments cannot confirm if the mole necessarily uses the physics we have described to stabilize bubbles during underwater sniffing. Even so, we believe the results of this study will be important in designing an end-effector for a mole-inspired underwater sniffing electronic nose.

Future experimental changes could allow closer comparison to the star-nosed mole's sniffing. The star mimics in our study were flat, with fin-like arms, but one could investigate the effect of changing the angle at which the arms deviate from this plane to form a concatenated cone and mimic the way the star-nosed mole cages the bubbles during sniffing, using rods instead of fins. It is also important to consider the wettability of the mole's appendages, as hydrophobic surfaces are very effective at stabilizing large bubbles [35]. Lastly, the star-nosed mole appendages are flexible and clearly bend when in contact with the bubble. Such effects may increase the stability of the bubble, as the bending of the arms would increase the contact with the bubble and the required force to cause the bubble to escape.

The experiments and theory presented consider only a static case, but the sniffing per-

formed by star-nosed moles is a dynamic event. Future work should consider the effect that the star geometry has on bubble formation and retraction. Specifically, it would be interesting to quantify the delay to pinch-off caused by the star and how the bubble surface is altered during that time-scale, as the sniff duration and bubble surface area are critical in understanding the star-nosed mole's capabilities in capturing odors.

The star geometry is unique to the star-nosed mole, yet the American water shrew and Russian desman have shown similar underwater sniffing capabilities. It is possible that the whiskers of these animals could serve an analogous role to the star-nose in stabilizing the bubble. Moreover, it is likely that a number of other mammals may use this ability to smell underwater. A greater understanding of the mechanisms that stabilize the bubble in underwater sniffing may help in identifying other mammals capable of this intriguing behavior.

2.4 Methods

We give a detailed description of the star-fabrication process as well as our detailed calculation of bubble volumes for the small gap theory.

2.4.1 Star fabrication

Plastic stars are designed in Solidworks. We begin with a circular disc of radius 20 mm. We then cut a central hole of radius $R_{nozzle} = 0.75$ mm, which corresponds to the dimensions of the syringe's nozzle. Around this hole, a ring of solid plastic, of outer radius $R = 3.5$ mm forms the center of the star. Triangular arms are cut extending from this ring, by considering both the gap angles desired and the strength of the material. Ultimately, we designed 5 arm designs, with gap angles θ of 0°, 3°, 8°, 15°, and 20°, respectively, as shown in **Figure 2.8b**. Note that a gap angle of 0° denotes a complete disc with no gaps. **Figure 2.8c** shows the relationship between the number of gaps n and the gap angle θ of the star. The stars we designed are represented by the blue points. Our first constraint is

based on the strength of the material. Each arm of the star must have a minimum width of $L = 2$ mm so that it is not melted off during the laser-cutting process. This constraint may be written

$$\left(\frac{2\pi}{n} - \theta\right) R > L, \tag{2.8}$$

and is shown by the red dashed line in **Figure 2.8c**. As we found from experience, any stars that fall above this dashed line will break, at least if they are constructed from transparency sheet material.

The other constraint is on the ability of the stars to contact the bubble. In our preliminary tests, we found that we need as many gaps as possible to ensure that the bubble is forced to interact with the gaps. Moreover, we also desire an even number of gaps to maintain both front-back and left-right symmetry of the star. To determine the number of gaps cut into the star, we start at the fabrication limit and choose n to be the highest even integer below that curve. This results in stars with 6-10 arms rather than 22 arms, as in the star-nosed mole. In §3, we will use the following relationship between number of gaps and the gap angle:

$$n = -\frac{1}{3}\theta + 11. \tag{2.9}$$

This relationship is the best fit line considering the $3°$ and $15°$ stars, and is shown by the solid black line in **Figure 2.8c**.

To fabricate the stars, we begin with overhead projector transparency sheets composed of cellulose acetate. The material chosen is hydrophilic, as shown by the contact angle of $\xi = 54°$ in the inset of **Figure 2.3a**. We cut the star patterning using a laser cutter (Trotec Speedy 3000) into the various shapes shown in **Figure 2.8b**. A star is then super-glued onto a 3-mL syringe, which is in turn tied to the arm of a protractor so that it can freely swing in one plane. We orient the star so that the gaps of the star maintain symmetry both in this plane (left-right symmetry) and perpendicular to the plane (front-back symmetry, or symmetry into and out of the page in **Figure 2.3a**). Front-back symmetry is preferred

because it allows us to accurately characterize the bubble shape from a single view, and to perform modeling with fewer variables. Left-right symmetry is maintained because we perform tilting experiments both to the left and to the right in order to obtain more data from the same star.
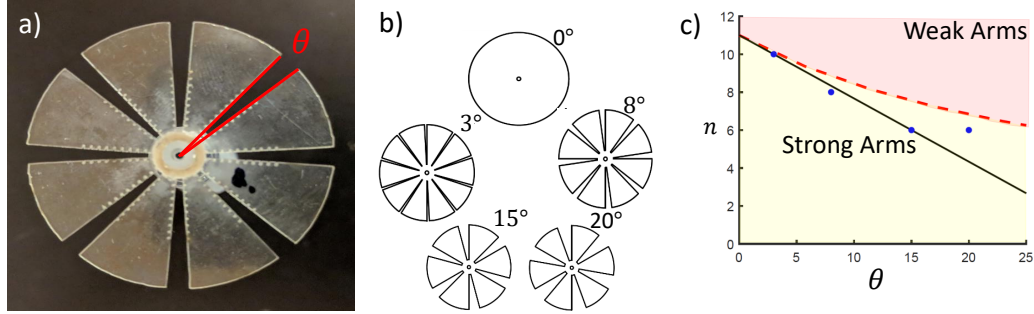
Figure 2.8: Design of plastic stars mimicking the star-nosed mole's nose. (a) Plastic stars laser-cut to mimic the star-nose. Like in the photos of star-nosed moles, the gap angle was measured along the inner edges of the arms with the vertex at the center of the nozzle. (b) Schematics of the five plastic stars used in this study. Angles indicate the gap angles for each of the stars. (c) Relationship between the gap angle θ and the number of gaps for each star. The dashed red curve represents the fabrication limitation that the minimum width of each fin is greater than 2 mm. The blue dots are the actual number of gaps used in the experimental stars. The solid black line is a linear approximation used to represent the relationship between the number of gaps and the gap angle for smaller gap angle stars from $3° - 15°$.

To demonstrate the stabilizing physics of the stars in an alternate way, we also fabricate a disc with no gaps that deforms the bubbles in a two-dimensional manner, as shown in Figure 2.6. A plastic disc is creased at a distance 3.5 mm from the center of the nozzle. The crease is made so that the disc exhibits a bend of angle $\zeta = 15°$.

2.4.2   Bubble component volume calculation

We calculate the volumes v and V for the small gap theory. We write the volume $v = v_1 + v_2$ where the volumes v_1 and v_2 are labelled in **Figure 2.5b**. We approximate the region v_1 as a pyramid, requiring the area of the base and the maximum height of the bubble to calculate

its volume. The base is written as

$$b = \frac{\theta}{2\pi}[\pi(\Delta R_r + R)^2 - \pi R^2].$$ (2.10)

If there are no gaps, then $\theta = 0$, and there is no counterweight bubble.

To find the height of v_1, we first calculate the curvature of the bubble rising through the gap according to the Young-Laplace equation

$$C = \frac{\Delta p}{\sigma}$$ (2.11)

where σ is the surface tension at an air-water interface and Δp is the difference in pressure between the surrounding water and bubble, $\Delta p = \Delta \rho g z$. From photographs, we measured the bubble angle at the plastic-water-bubble interface to be $\psi = 127°$. If we consider the cross-section of this volume as a concatenated circle, then we get the height

$$h = \frac{1 + \cos \psi}{C}.$$ (2.12)

The height h, was also measured from photographs and was found to be similar to our theoretical calculation. With h, we calculate the volume of the bubble peeking out through a gap in the star

$$v_1 = \frac{1}{3}bh.$$ (2.13)

To calculate v_2, we approximate the entire bubble below the star to be the shape of a cylinder. In that case,

$$v_2 = bd$$ (2.14)

where d is the depth of the cylinder. This depth is given by the contact angle ξ and the

capillary length λ_c[41][42]

$$d = \sqrt{2(1 - \cos(\pi - \xi))\lambda_c^2}. \tag{2.15}$$

With values for v_1 and v_2, it is simple to calculate v, keeping in mind that the volume of bubbles in the receding half of the gaps act as counterweights. The remaining volume of the total is V, whose buoyant force is the cause of pinch off

$$v = \frac{n}{2}(v_1 + v_2) \tag{2.16}$$

$$V = V_t - v \tag{2.17}$$

If we substitute equation **Equation 2.17** into equation **Equation 2.6** we have

$$\rho g(V_t - v)\sin\phi \le \rho g v. \tag{2.18}$$

We can then substitute **Equation 2.13** and **Equation 2.14** into **Equation 2.16** to get an expression for v and then substitute **Equation 2.16** into **Equation 2.18**.

$$\left(V_t - \frac{n}{2}\left(\frac{1}{3}bh + bd\right)\right)\rho g \sin\phi \le \left(\frac{n}{2}\left(\frac{1}{3}bh + bd\right)\right)\rho g \tag{2.19}$$

where b is a function of both the gap angle θ and tilt-angle ϕ. **Equation 2.19** gives this relationship between ϕ and θ, shown by the dashed red curve in **Figure 2.3b**.

23

CHAPTER 3

INTESTINES OF NON-UNIFORM STIFFNESS MOLD THE CORNERS OF WOMBAT FECES

3.1   Introduction

In our previous chapter, we saw how divots in the star nosed bubbles can help stabilize it. In this chapter, we transition from gases to solids, and examine the formation of corners in a wombat's feces. After considering the area minimizing effects of surface tension in bubbles and other soft materials, it is surprising to find corners appearing in soft objects in nature. As we will see in this chapter, the wombat uses a combination of intestinal material properties and repeated contractions to form these corners.

The ability of wombats to form relatively uniform, clean cut, cubic feces–as opposed to the tapered cylindrical feces of most animals– is unique in the animal kingdom. The earliest documented observation of wombat cubic feces is by Eric Guiler (1960), who states: "The droppings of wombats are of a characteristic rectangular shape" [43]. The next publication dates 1979 [44], although the droppings were known within Australia well prior to both these references. It is currently poorly understood how these animals produce geometric scats. With no immediately apparent explanation as to how an animal's defecation process could produce cube-shaped scats, a range of hypotheses have been proposed over decades [45, 46, 47]. A sample of hypotheses include compression of fecal material between pelvic bones, a relatively geometric-shaped sphincter, and parallel blocks of longitudinal intestinal smooth muscles in the cecum. Notably, all hypotheses have exclusively remained the matter of objective speculation and assumed mechanism, rather than subject to actual investigation.

The ability of wombats to form cubic feces is of both general and practical interest.

How animals engage in varying forms of communication, and the underlying evolutionary forces driving them, have been of interest to ecologists for decades. Recent fluid dynamic modelling has investigated cylindrical scat formation [48], with clinical application to diarrhea and constipation disorders [49], however mechanisms leading to the formation of diverse fecal shapes is less understood. In the built world, cubes and shapes with sharp edges are made by cutting, molding or extrusion. Examples include extruded pasta, hay cubes and injection-moulded plastics. Cube formation in animal models appears to be a new method, and may inform manufacturing processes, particularly if soft biological materials are of interest. Another application may be in the care of captive animals. In Australia, wombats are kept in captivity in zoos and wildlife parks, and their feces are cleared on a daily basis. Quantifying a wombat's scat shape may be a useful metric for non-invasively assessing the quality of a wombat's diet, digestive health, or level of hydration.

In this study, we will focus on the bare-nosed wombat *Vombatus ursinus*, which produces the most cubic feces of the three species of wombat. The bare-nosed wombat, shown in **Figure 3.1a**, has an adult body length 1 m and mass 20-35 kg. It is drought-tolerant and lives a solitary lifestyle in underground burrows. It typically produces 80-100 cubic feces per day mostly above ground [45]. Wombats generally have low-nutrient diets, primarily consisting of grasses and sedges [50]. To compensate, they have long, spacious intestines of length 6-9 m (See **Figure 3.1e**), utilize hind-gut fermentation, and have a mean food passage retention time of 40-80 hr [50, 51]. In comparison, a human of 100 kg has an intestinal length of 8 m, fore-gut fermentation, and a mean food passage retention time of 50 hr [52, 53]. The extended digestion period of wombats allows them to maintain exceptionally low metabolic rates [54, 55] and also an energetically expensive digging lifestyle [56]. These attributes allow the wombat to survive droughts that would challenge most other mammals.

Animals have long been known for using their urine and feces to communicate. However, wombats have a unique way of using their feces as markings. Wombats, particularly bare-nosed wombats, have a propensity to deposit feces in aggregations called latrines.
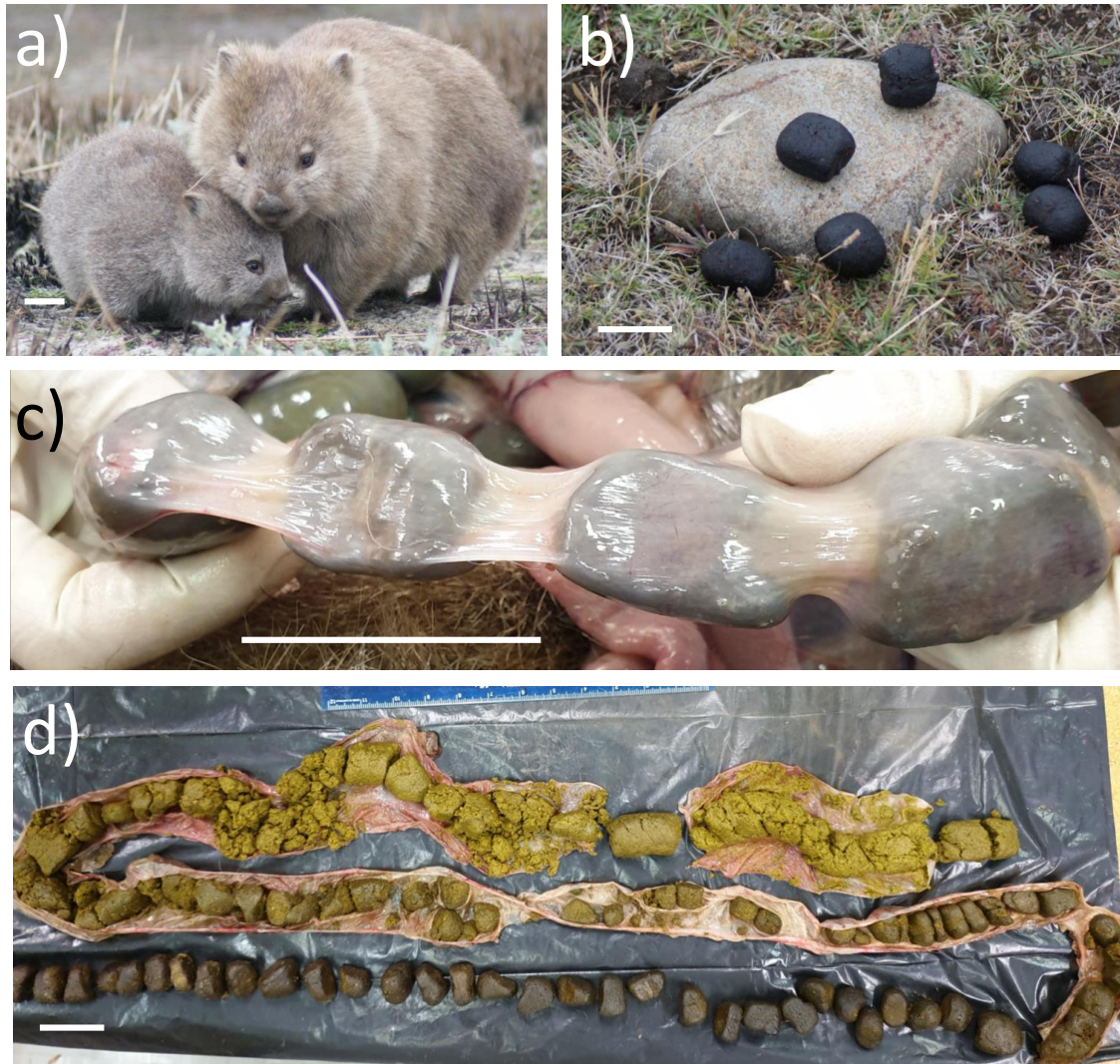
Figure 3.1: Wombats form cubic feces. All scalebars represent 5 cm. (a) A female wombat with her joey. (b) A typical wombat latrine consisting of feces placed on a low rock or stump. (c) A 2019 dissection of a wombat shows the cubic feces fully formed within the mid-distal colon, (d) The excised 3 m of wombat intestine shows feces transforming from a yellow yogurt-like slurry near the stomach to darkened dry cubes near the anus.

Such latrines are found on or next to distinctive landscape features such as prominent rocks, logs and small rises, and burrow entrances within their home ranges [45, 57], as shown in **Figure 3.1b**. Latrines are generally found with five or more wombat scats indicating that one or several wombats may be involved. It is generally believed that prominent latrines facilitate visual or olfactory communication between wombats or other nearby animals. It has been proposed that the flat sides of the feces serves the purpose of latrine stability by preventing the feces from rolling off these raised surfaces [45, 46, 47]. Understanding how wombats produce cubes may provide insight into how such a unique adaptation evolved.

In this study we investigate cube formation in the wombat using dissections, material measurements, and mathematical modeling. We begin in section 2 with the histological and tensile experiments performed on wombat intestine samples as well as 2D phenomenological modeling informed by these experiments. In section 3, we discuss the implications of our work and provide suggestions for future research. In section 4, we summarize the contributions of our study. In section 5, we provide the detailed methods.

3.2   Results

3.2.1   Wombat experiments

Among Australians, a popular hypothesis is that wombats produce cubes by extruding feces out of a square anal sphincter. In 2019, we obtain a CT scan of a live adult female wombat. The scan shows that the wombat's anus is round, a feature consistent with all other animals. Also, the pelvic bones, which the feces were once proposed to glide past, are nowhere in the vicinity of the colon. We thus conclude that wombats do not change their feces shape through extrusion. We obtain further evidence that extrusion does not influence shape with a series of dissections of wombats.

In this study, we present data from three dissected wombats, all obtained following euthanasia by veterinarian owing to vehicle collisions in 2018-2020. Unfortunately, vehicle collisions are a source of wombat and other marsupial mortality events in Australia. In

2018, we dissect a young female wombat (2-3 years old). In 2019, we dissect an adult male wombat (> 2 years old). And in 2020, we dissect a young male wombat (< 2 years old). Given the similarity in age and size of all wombats, we expect feces and intestinal measurements to be comparable. All dissected wombats are referred to by the year of dissection. From the 2018 wombat, cubic feces are removed from the end of the distal colon and unformed feces removed from the end of the proximal colon.

The wombat intestine of 6-9 m length (approximate length for a fully grown wombat) consists of four sections after the oesophagus: these include the stomach (0.14 m), a relatively short small intestine (3.2 m), long proximal colon (3.9 m) and distal colon (last 1.8 m). **Figure 3.1d** shows the shape of feces with relation to their position in the intestine (lower proximal colon to lower distal colon). In the proximal colon, the feces are a yellow-green slurry of digesta. As the fecal material approaches the anus, it becomes increasingly dry, as shown by the darker color. The beveled edges and flat faces also become increasingly prominent.

The removal of water from the feces may help it to better retain its shape. Generally, at higher solid fractions, mammalian feces are more viscous and behave viscoplastically [58]. To measure the level of dryness we begin by removing feces samples from both the proximal and distal colons. By weighing a scat, we obtain m_{wet}, and by drying them in an oven, we obtain m_{dry}. We define the water content of each sample using $w = \frac{m_{wet} - m_{dry}}{m_{wet}}$. Feces from the proximal colon have a water content of $w = 0.81$ and show an amorphous shape. Feces from the distal colon, the last 1 m (or 17 percent) of the 6 m digestive tract, have a much lower water content of $w = 0.53$. This water content is lower than many mammals: for example, humans have a fecal water content of $w = 0.74$ [59].

The fecal cubes have dimensions: height 2.3 ± 0.3 cm, width 2.5 ± 0.3 cm, and axial length 4.0 ± 0.6 cm (See **Figure 3.2**), and the edges of the feces are beveled. Thus, the aspect ratio of the feces is 1:1:1.6, and so technically the feces are rectangular prisms, but for simplicity, we continue to refer to them as cubes in this paper.

To understand the formation of the cubes, we hang an intact intestine vertically allowing the bottom end to swing and rotate freely. We observe that the corners of the cubes are aligned, suggesting that the intestine itself has a coordinate system to dictate corner formation. We hypothesize that this coordinate system is written in the intestines in terms of its thickness and its material properties. To explore this idea, we turn to histology and material testing.
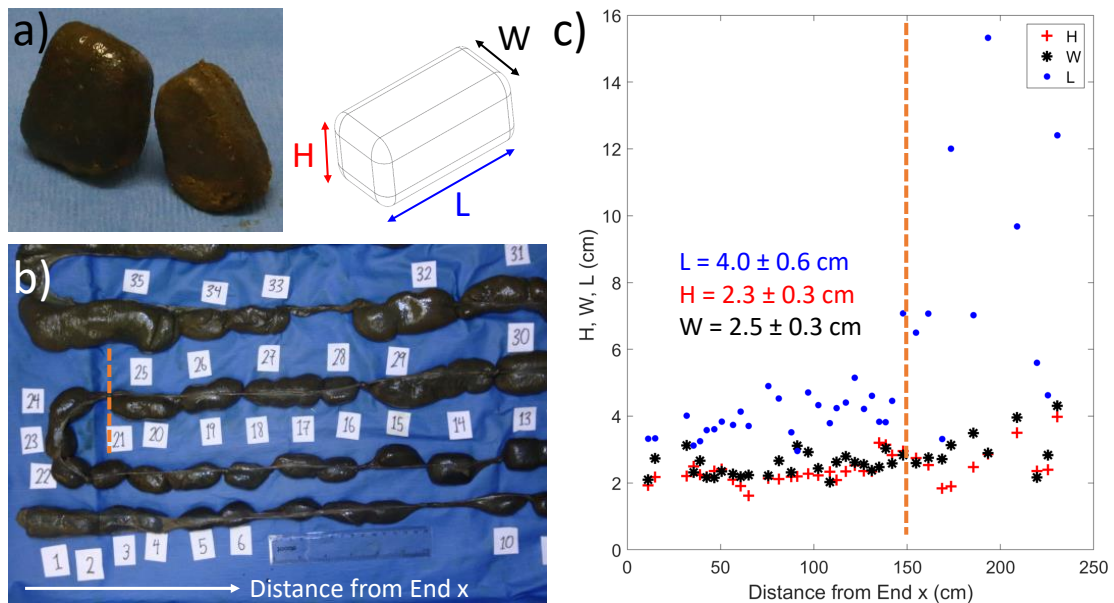
Figure 3.2: Feces measurements from 2018 dissection. a) Measured feces length, height, and width inside the intestines. b) Location of feces within intestines measured as distance from the anus. Orange dotted line marks 1.5 m from the anus. c) Last 1.5 m shows dimensions becoming consistent at $4 \times 2.3 \times 2.5$ cm.

3.2.2   Material properties of wombat intestine

From the 2019 wombat, two cross sections of the intestines are hematoxylin and eosin stained and the thickness of the tissue layers are measured under a microscope. Since the cubes form in the distal colon, and are amorphous in the proximal colon, we obtain cross sections from both the proximal and distal colon and perform histological staining. These sections are 50 cm and 200 cm away from the anus. We observe the four major

tissue layers, arranged external to internal: longitudinal muscle, circular muscle, glandular tissue, and mucosa, as labelled in **Figure 3.3ab** with the letters L, C, G, M, respectively. In particular, the circular and longitudinal muscle thickness varies greatly between different azimuthal locations, and so we focus on these two layers from hereon.

Figure 3.3cd shows the relationship between tissue thickness and azimuthal position in the proximal and distal colon. We arbitrarily assign $\theta = 0°$ as the position of observed lowest thickness of the intestine. The longitudinal muscle, the circular muscle, and the total thickness of both muscles are shown by the blue, red, and black lines, respectively. Examining the distal colon section first, shown in **Figure 3.3d**, the longitudinal tissue layer more than doubles in thickness, from 10 μm to 25 μm, with the peak occurring at $\theta = 270°$. The circular muscle also has a 50% increase from 22 μm to 35 μm, with peak at $\theta = 90°$. It is noteworthy that the peaks are $180°$ out of phase, as shown by the the total thickness, which has peaks at $90°$ and $270°$.

As shown in **Figure 3.3c**, the proximal colon also has two peaks. The azimuthal location may not match that of the distal colon because we could not maintain azimuthal alignment between the two sections. The presence of thickness peaks combined with the absence of the cubic feces in the proximal region indicates to us that both feces dryness and intestinal properties must be present to enable cubing to occur.

From the 2020 wombat we test the tensile material properties to determine the effects of non-uniform tissue thickness. We cut two sequential cross sections of the distal colon to perform material testing. These circular bands are cut $180°$ out of phase so that we can obtain data in regions that have been clamped during the testing (See **Figure 3.3ef**). We perform tensile testing to measure stiffness as a function of azimuthal position. We infer stiffness by the strain measured between lines drawn at increments of 4 mm. **Figure 3.3g** shows the relationship between stiffness and azimuthal position, where the blue and red points are stiffness from each of the two cross sections, and the black is the average stiffness of each $30°$ region. We observe a single peak in stiffness at $\theta = 90°$ in the distal colon,
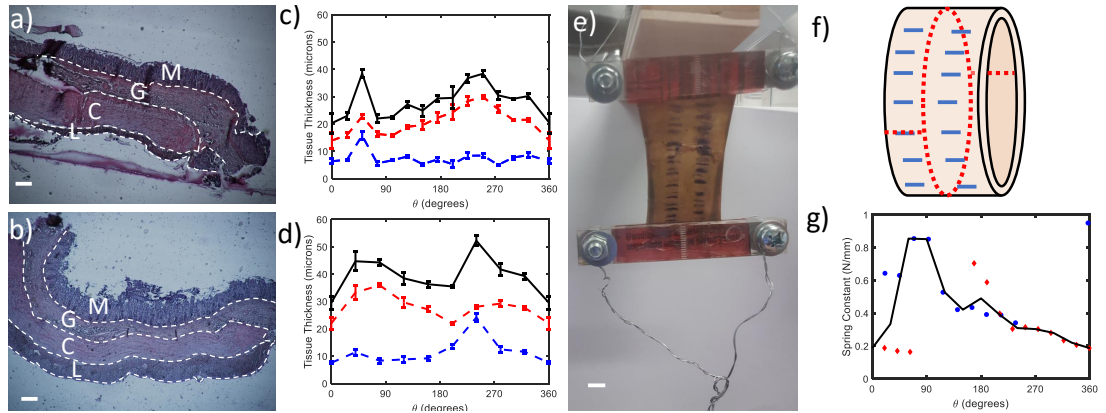
Figure 3.3: Non-uniform thickness and stiffness of the wombat intestine. (ab) Histology of the distal colon, with the longitudinal muscle, circular muscle, glandular tissue, and mucosa layer labelled with the letters L, C, G, M, respectively. Scale bar, 20 microns. (a) Staining corresponds to the azimuthal position $\theta = 40°$ and shows the thinnest longitudinal muscle thickness. (b) Staining corresponds to $\theta = 240°$ and shows the largest longitudinal thickness. (cd) The relationship between azimuthal position and tissue thickness, with the longitudinal muscle, circular muscle and total muscle thickness given by the blue, red, and black lines, respectively. (c) is from the proximal colon, and (d) from the distal colon. (e) Custom-built tensile testing setup for the wombat intestines. Scalebar, 1 cm. (f) Schematic showing two sequential cross sections cut at $180°$ offset to obtain tensile testing data of the full $360°$. Cuts are made at the dotted red lines and tick marks are drawn using the blue lines. (g) The relationship between azimuthal position and tissue stiffness. The blue and red points correspond to each of the adjacent cross sections and the black line to the average stiffness.

where $\theta = 0°$ is set to be the location of lowest stiffness. Because the two cross sections are sequential we expect them to have comparable trends. Wide discrepancies in the data near $\theta = 0°$ and at $\theta = 180°$ are likely due to the tissue being clamped near those regions, which affects its ability to stretch laterally, affecting the stiffness measurement.

3.2.3   Simulation of intestinal contractions

We continue with our study using a theoretical model that assumes that there are two bands of increased stiffness located $180°$ out of phase. Tensile testing of passive tissue only displays a single stiff region, but this test only measures azimuthal stretching. A peristaltic contraction relies upon muscles in both the azimuthal and the longitudinal directions. We surmise that the peak in stiffness observed in the tensile test may correspond to the factor of three increase thickness in the longitudinal muscle. The 0.5 factor of increased thickness in the circular muscle apparently was not detected by our tensile test. We hypothesize that the increased circular muscle thickness results in a locally stronger muscle contraction during peristalsis. This locally increased contraction would phenomenologically be similar to an increased stiffness. For simplicity, we develop our model as having two stiff regions to represent the increased thickness of longitudinal and circular muscles. An important parameter in this model is the stiffness ratio C, the ratio between maximum and minimum stiffness, which we observe in our tensile tests to be 4 (See **Figure 3.3g**, peak stiffness is 4 times that of baseline stiffness).

We propose a phenonemological model to investigate how non-uniform intestinal properties can influence feces shape during peristaltic contractions. The goal of our model is to rationalize how two regions of stiffness can result in four corners of the feces. A square is defined as having 8 regions of differing curvature: zero curvature at the flat sides, and steep peaks at each of the corners. It is thus not obvious how the contraction of a band with 2 regions of stiffness can result in 4 peaks in curvature.

We begin with a few caveats on our model. The real wombat intestines are three-

32

dimensional and filled with viscoelastic feces. The peristaltic contractions occur at an un-known intensity for an unknown duration. Thus, a fully accurate three-dimensional model cannot be done with the current knowledge about the intestine material dynamics. Instead, we take a simplified approach: our model is two dimensional, considering a circular cross-section of the intestine. Rather than modeling the interaction between the intestines and the viscoelastic feces, the feces are represented as added mass along the intestinal walls as well as a linear damping in all directions.

We conduct our modeling in two phases, beginning with an equilibrium phase to create an initial strained state of the intestine, and followed by a non-equilibrium series of contractions. In the first phase, feces are initially pushed into the 2D cross-section of our model. We assume the feces exerts a constant pressure against the intestinal walls until the system comes to equilibrium. We find that this equilibrium state is necessary to prevent unphysical behavior in the second phase of the model.

Once the initial equilibrium state of strain is found, the intestine begins contracting by shortening the springs' rest length, l_0. Multiple contractions are simulated by changing the rest length to a contracted value, holding the contraction, and then taking a relaxed value, and holding this length. The contraction dynamics are thus idealized as a square wave. The governing equations arise from the damping force in all directions and the elastic spring forces of the intestinal walls. The evolution of the solution shape is recorded as a function of time. Since the wombat feces change shape as it travels down the intestine over 2-4 days, it is not clear whether it reaches an equilibrium shape before it is ejected. Thus, our goal is not to find an equilibrium shape for the feces but to record how transient square-like shapes can arise. We also use this method to determine how different intestinal and fecal parameters may influence the shape.

Now that we have discussed the general idea of the model, we turn to the specifics of the implementation. We divide the intestine into a ring of $4n$ nodes, each of mass m. Each node is connected to its neighboring nodes using linear springs of varying stiffness. We

divide the ring into 4 quadrants of n nodes each. The regions are sequentially soft and stiff in an alternating ABAB pattern, shown in **Figure 3.4a**, and similar to the variation in thickness we observe from the wombat histology. The soft zones have springs of stiffness $4nk$, and the stiff zones have stiffness of $4Cnk$, where the stiffness ratio $C > 1$. Including n as a factor in the stiffness allows the overall stiffness of the system to be independent of the number of nodes in the ring.

To find the initial configuration for the model, we solve for the equilibrium state. This state will depend on the minimum and maximum spring stiffness $4nk$ and $4Cnk$, and the spring lengths l_i. It does not depend on mass or damping, which arise in the contraction phase. As the feces are pushed into the 2D intestinal ring, it exerts an outward constant pressure P.

The equilibrium arrangement of nodes is found from the local force balance on the individual nodes. Consider a node within the soft region (See **Figure 3.4b**). Attached to it are two springs of stiffness $4nk$, stretched to lengths l_1 and l_2, respectively. The angle formed between the springs is ϕ. The pressure force exerted on the node is perpendicular to the spring and proportional to the spring length, $\frac{1}{2}Pl_1$ and $\frac{1}{2}Pl_2$. We draw our axis parallel and perpendicular to the angular bisector. By considering the force balance perpendicular to the angular bisector, we see that $l_1 = l_2$. This also holds true for nodes within the stiff region. We can also show that if all of the spring lengths are the same, the angle ϕ of each of those nodes must also be the same.

We then have 5 unknowns: l_A and ϕ_A for the soft regions, l_B and ϕ_B for the stiff regions, and ϕ_{AB}, the angle at the 4 interfacial nodes between the stiff and soft regions. We therefore require 5 equations. Four equations come from local force balances, and the final equation comes from the assumed convex geometry of the equilibrium shape. This calculation is described in more detail in section 5.

The equilibrium shape is used as the initial condition of the intestine before the contraction begins. The contraction of the intestinal wall is simulated by alternating the rest

length of each spring from l_0 to $l_0/4$ using a square wave with period τ. As wombat intestine contractions occur at an unknown intensity and period, these parameters were chosen arbitrarily.

$$l_0 = \begin{cases} l_0 & \cos(2\pi t/\tau) < 0 \\ l_0/4 & \cos(2\pi t/\tau) \geq 0 \end{cases} \tag{3.1}$$

The net force comes from the two spring forces attached to each node and a damping force $-b\vec{v}_i$ opposing the direction of motion, where b is a damping coefficient and $\vec{v}_i$ is the velocity of the ith node. The mass of each node, m accounts not only for the mass of the intestinal tissue, which is likely negligible, but also the added mass of the feces as it is displaced along the digestive tract.

Figure 3.4cde shows the progression of wombat feces shape during a series of contractions, using $n = 50$ nodes for each region, a stiffness ratio $C = 4$, damping $b = 45$ g/sec, and added mass $m = 0.045$ g. **Figure 3.4fgh** shows the curvature measured around the feces. The initial equilibrium shape of the intestine is fairly circular, as shown by the nearly constant curvature in **Figure 3.4f**. **Figure 3.4d** shows the peak squareness during mid-contraction, where the feces shows the start of 4 corners, and the curvature in **Figure 3.4g** shows 4 peaks. The intestine displays this transient square state and then passes out of the square state as the contractions continue. We show a point later in the contractions in **Figure 3.4eh** showing the feces is clearly less square.

3.2.4 Simulation analysis

While it is easy to qualitatively distinguish between circles and squares in both the simulation shape and the curvature, $\kappa(\theta)$, graphs, we require a way to quantitatively measure the squareness of the shape. There exist many simple methods to measure how round an object is [60], and we find one potential way to measure squareness based on the definition of the squircle [61]. However, the method based on the squircle definition is not robust to the noise found when applied to natural wombat feces. It evaluates most samples as very
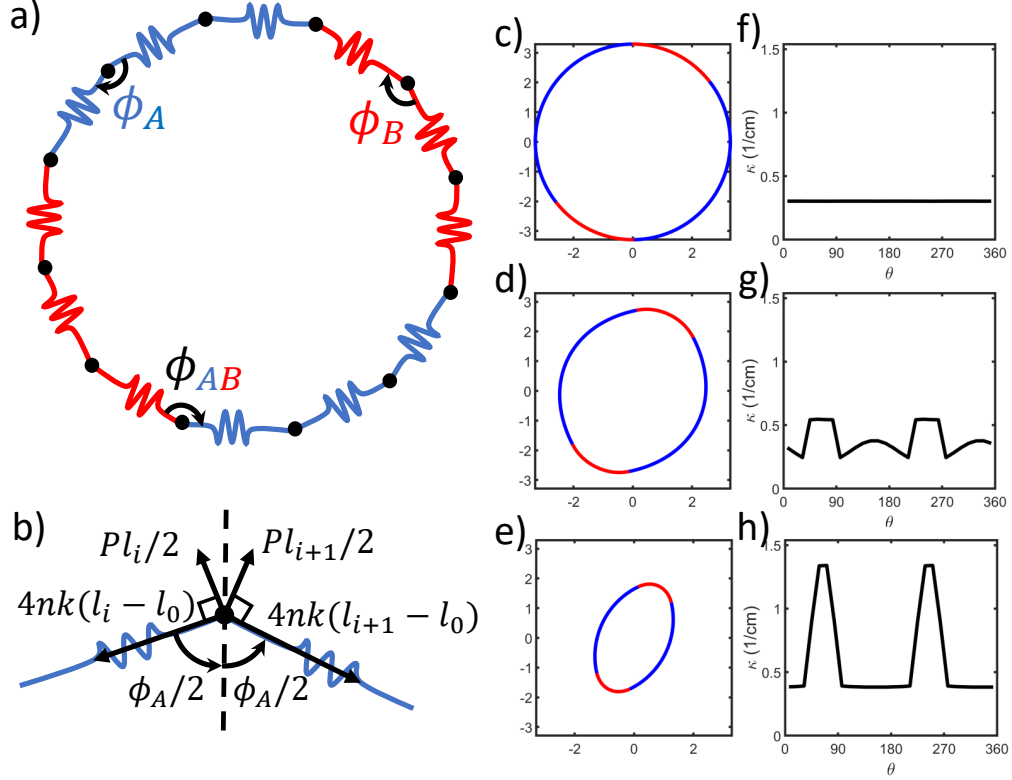
Figure 3.4: The mathematical model of contracting wombat intestines. (a) Schematic of the elastic ring simulating the intestine. Blue and red regions indicate low and high stiffness zones, respectively. This color scheme is valid for (c-e) as well. (b) Close-up of the variables defined at a single node. The equilibrium shape of the intestine arises from solving the force balances perpendicular and parallel to the angular bisector shown. (c-e) Sequence of intestine shapes during a series of contractions and the corresponding relationships (f-h) between curvature and azimuthal positions for each of these shapes. For these simulations, $C = 4$, and Re = 10^{-3}. (c) At time $t = 0$ sec, the equilibrium shape is close to circular, and the curvature (f) is near constant. (d) After several contractions, the intestine becomes increasingly square ($t = 7.9$ sec), as shown. Note that depending on the Reynolds number and stiffness, some shapes are are more square than others. The four peaks curvature in (g) correspond to the four corners. (e) Past the peak squareness, S, the contraction continues to deform the intestine, and the shape begins to resemble an ellipse. This frame corresponds to a time $t = 30$ sec.

square, but for a few, visually similar samples, it evaluates them as very round.

We proceed by proposing a squareness metric that employs the $\kappa(\theta)$ signal and cross-correlates it to idealized reference curvatures going from the flat curvature of a circle to the infinitely peaked curvature of a square (See **Figure 3.5a**). Our final squareness S is defined in **Equation 3.17** in the Methods section, and varies between 0 and 1, with 1 as being most square.

Figure 3.5b shows the time course of feces squareness during the simulation. We perform 40 sequential contractions, with each oscillation in the figure marking a contraction. The squareness has a sharp increase at $t \approx 5$ sec with a peak squareness of $S = 0.3$ at $t = 7.9$ sec. Subsequently, the squareness decreases, demonstrating the transient nature of the square shape in the simulation.

To determine if our simulation captures the squareness of actual wombat feces, **Figure 3.5c** shows 36 wombat feces collected around Maria Island, off of Tasmania, Australia. A histogram of the squareness of these samples is shown in **Figure 3.5d**, and we find that the feces have a mean squareness of 0.14 with a standard deviation of 0.1. These lower values appear to be due to sensitivity to the shape's aspect ratio. For rectangular shapes, the corners are not spaced apart azimuthally in a way that matches the reference curvature. Nevertheless, our metric gives similar values to visually similar shapes. We proceed by using our squareness metric to explore the effect that different simulation parameters have on the resulting feces shape.

We consider two dimensionless groups as the independent variables that characterize the intestinal contraction: the stiffness ratio C, and the Reynolds number, Re. The stiffness ratio is defined as

$$C = \frac{\text{stiffness of stiff region}}{\text{stiffness of soft region}}, \tag{3.2}$$

where we observe wombat feces has a stiffness ratio of $C = 4$. We conduct simulations by matching simulation Reynolds number Re with the biological Reynolds number, defined as
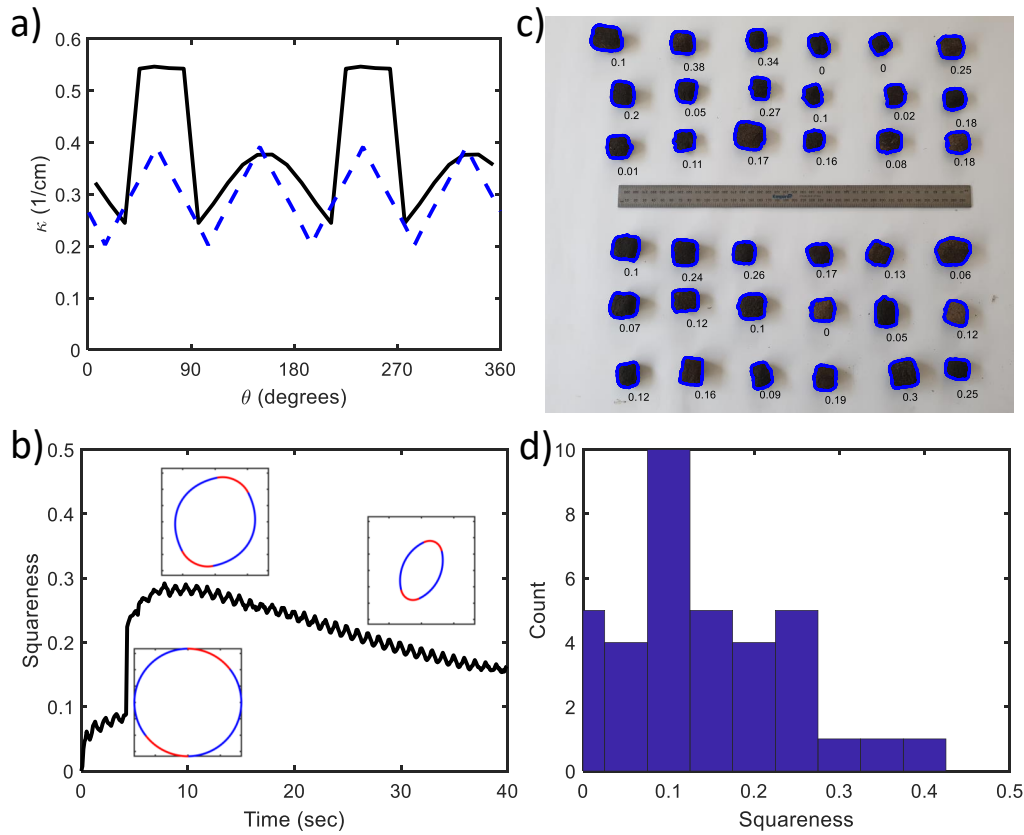
Figure 3.5: Squareness for simulated and actual wombat feces. (a) The relationship between curvature and aziumthal position. The curvature at one point in time ($t = 7.9$ sec) during a contraction is shown by the black solid line. To evaluate squareness this curvature is correlated to the corresponding reference curvature shown by the blue dotted line. The reference curvature shape is defined using the variable λ. Decreasing λ corresponds to greater peaks in curvature, and greater squareness S. (b) The time course of squareness S during a series of intestinal contractions. Insets show the simulation shape at t=0, 7.9, and 30 sec. The oscillations in squareness correspond to each contraction. (c) An array of 36 wombat feces picked from Maria Island in Tasmania for their exceptionally cubic shape. The blue outlines indicate the measured shape using image analysis. The numbers below each feces correspond to the calculated squareness. (d) A histogram of squareness of natural wombat feces from part (c), demonstrating a mean squareness of 0.14 and a standard deviation of 0.1.

$$\mathrm{Re}_b = \frac{\rho L v}{\mu} = \frac{\text{inertia}}{\text{viscous force}}, \tag{3.3}$$

where ρ and μ are the density and dynamic viscosity of the feces respectively. We focus on the Reynolds number characterizing the peristaltic contractions that generates the square cross section, and not the Reynolds number of the slower axial flow through the intestines. Therefore, L is the radius of the intestine and v is the radial velocity of the intestine during a contraction. For the feces of mammals [48], $\rho \approx 1~g/cm^3$ and μ varies between $10^3 - 10^5$ g/(cm sec). The radius of the wombat intestine is on the order of unity, $L \approx 1$ cm. Based on the peristaltic contraction frequency of dogs and humans [62], which are between $f =$ 0.05-0.2 Hz, we approximate that wombat intestine contractions have a characteristic radial velocity of $v = fL$ = 0.01 - 1 cm/sec. All together, we approximate the Reynolds number of wombat intestines deforming feces to be $\mathrm{Re}_b \approx 10^{-7} - 10^{-3}$. Since wombat feces is drier than that of most mammals, the Reynolds number may be even lower, especially near the anus.

Since our simulation is two-dimensional, and only accounts for the feces properties in a phenomenological manner, we must redefine the Reynolds number for the simulation. The length scale is the mean radius of the initial equilibrium intestine configuration, R. Similar to the biological system, the radial velocity is $v = R/\tau$, where τ is the period of the model contractions. Note that the radius, and thus the velocity, are functions of the spring constants, with higher spring constants associated with a smaller equilibrium intestine size. The 2D density is calculated as the added mass divided by the radius squared, $\rho_{2D} = m/(R^2)$, which has units of mass per unit area. The viscosity of the feces is taken as the viscous damping coefficient b, which has units of mass/time. The simulation's Reynolds number is

$$\mathrm{Re} = \frac{(m/(\pi R^2))R(R/\tau)}{b} = \frac{m}{\pi b \tau} \tag{3.4}$$

To encapsulate the biological Reynolds number, we run simulations in the range of Re

$= 10^{-4} - 10^0$. Our first claim is that the two stiff regions found in the wombat's intestinal tissue serve an important role in forming the transient square state. We investigate this by performing a 1D parameter sweep of the simulation, varying the spring stiffness ratio C, which relates the maximum and minimum stiffness of the intestine, while keeping the Re $= 10^{-3}$. As C increases, the feces increases in squareness S according to the linear regression $S = 0.02C + 0.2$, $R^2 = 0.98$ (See **Figure 3.6b**). For comparison we include our experimental data by the open symbol, associated with a stiffness ratio $C = 4$ and a squareness $S = 0.14 \pm 0.1$. According to our simulations, this stiffness ratio would yield a squareness of $S = 0.28$, which is twice as large as the field data.

We now use our simulation to address the question of how four peaks in curvature result from only two peaks of stiffness. First consider a uniformly stiff ring. By definition, a smaller circle has higher curvature than a larger circle. Therefore, contracting a uniform ring of springs will naturally cause an increase in curvature.

Now consider contractions of a ring of non-uniform stiffness. In a zone of stiffer springs, an increase in curvature will occur earlier than for zones of softer springs. Since there are two stiff zones, this mechanism leads to two corners forming in the middle of the stiff regions. However, to get the remaining two corners in the correct location, there must be an increase in curvature in the middle of the soft regions as well. We propose that these corners form due to inertial effects at the center of the soft regions. As the stiff regions contract more forcefully, the neighboring nodes of these regions are also dragged towards the center. Conversely, the farthest nodes from the stiff regions are the middle nodes of the soft regions. Their added mass causes them to lag behind, creating an increase in curvature.

As evidence for this physical picture, we perform a parameter sweep in Reynolds number, shown in **Figure 3.6c**. The stiffness ratio is kept fixed at $C = 4$, and the Reynolds number is varied by manipulating the viscous damping b. As expected, the peak squareness of the simulations increases with Re. The simulation becomes less reliable for Reynolds number approaching 1, due to unphysical behavior such as the intestines crossing itself,
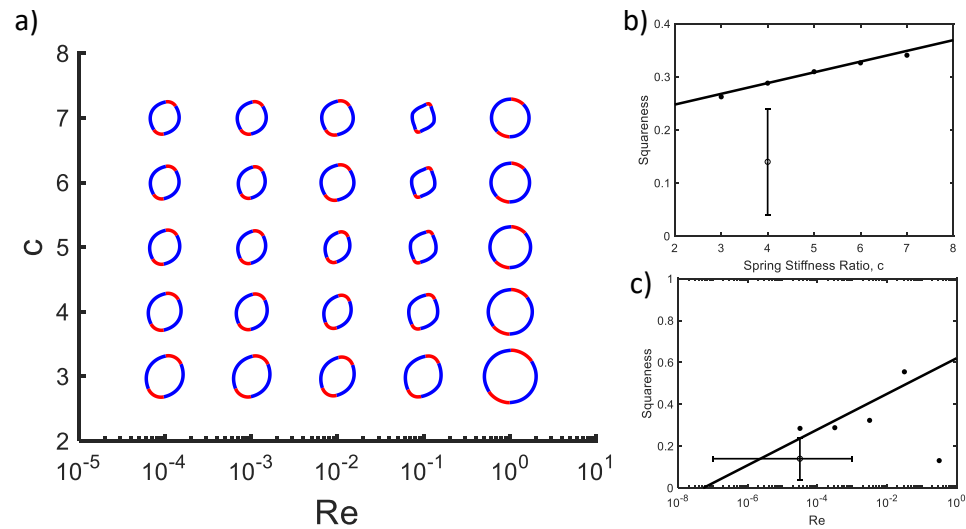
Figure 3.6: Regime diagrams of shape as a function of spring stiffness ratio C and Reynolds number Re. a) Qualitative 2D sweep of C and Re, showing the peak squareness in the simulation. b) The relationship between squareness S and spring stiffness ratio C, with solid points given by simulation and line given by linear best fit. The open symbol indicates the squareness of biological wombat feces, with error bars giving the standard deviation in the squareness. c) The relationship between squareness S and Reynolds number. Solid symbols give the simulation data, and open symbols denote the biological wombat squareness and our estimate for its Reynolds number.

41

which is permitted by the 2D nature of our simulations. Discounting the point at Re near 1, linear regression gives $S = 0.6 + 0.04 \log(\text{Re})$, $R^2 = 0.57$. The simulation show very shallow gains in squareness between $\text{Re} = 10^{-4} - 10^{-2}$, but then a significant increase in squareness at $\text{Re} = 10^{-1}$. **Figure 3.6a** shows the full 2D parameter sweep of both the spring stiffness ratio, C, and the Reynolds number. Generally, squareness improves for both higher spring ratios and higher Reynolds number, up to Re = 10^{-1}.

As an additional test of our proposed mechanism for corner formation, we consider the case of 3 periods of stiffness. With three stiff regions and three soft regions, we expect six corners to form. When running the simulation with three periods of stiffness, we expect a transient hexagon. While the hexagon is barely recognizable, its presence is illustrated by the six peaks in curvature (See **Figure 3.7**). That is to say, if an animal were to evolve 3 or 4 periods of stiffness along the circumference of their intestines, we predict that their feces would take the shape of hexagonal or octagonal prisms.
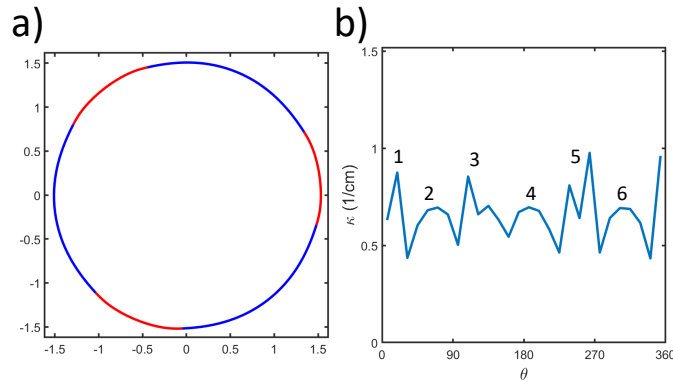
Figure 3.7: The results of simulation using 3 stiff regions. (a) A hexagonal feces is formed with barely noticeable corners. (b) The relation between curvature and θ, more clearly showing the six peaks in curvature in part a).

3.3 Discussion

In this study, we show that a combination of unique material properties and muscular contractions are necessary for wombats to produce feces with square cross sections. We discover the wombat intestines have non-uniform stiffness along the circumference, in part

due to variations in muscle thickness. When intestines conduct their regular peristalsis, digesta is moved towards the anus. Typical peristalsis is uniform in all azimuthal directions because the intestines themselves are uniform. However, the non-uniformity in the wombat intestines cause amplified contractions in distinct pre-set locations. Over many cycles, these non-uniform contractions, along with inertial effects, encourage the preferential movement of feces and the sculpting of the corners. While these inertial effects seem unlikely in a system with such a low Reynolds number, oscillatory motion may cause inertial instabilities at lower-than-expected Reynolds numbers [63]. The flat trend in squareness for simulations at $Re = 10^{-4} - 10^{-2}$ suggests that continued reduction of Reynolds number would have negligible effects on the squareness. Multiple contractions of short duration may reduce the magnitude of radial velocities and thus the damping, with respect to the damping of a single large longer contraction.

Our study shows corners forming in less than 10 contraction cycles. This early corner formation is not realistic because our model does not model the non-Newtonian nature of the feces. With contractions occurring every couple of seconds [62] over a time of 5 days [51], the feces actually experience on the order of 100,000 contractions. We believe that these missing details may explain why the model at the lowest Reynolds numbers only shows the initial formation of corners, especially in the soft regions, and why these corners never become sharp. We suspect that as the feces becomes drier, the yield stress nature of the material makes it increasingly capable of holding its cubic shape. Moreover, cubes are found only in the distal colon, and not the proximal colon, despite the periodic tissue thickness found in both regions. Future modeling that takes into account the effects of feces dryness might be able to resolve the onset of cubing in the distal colon.

In this work, we focus on the formation of the feces cross section, which involves four faces out of the six. We hypothesize that the axial length of the cubes is set by mechanical drying instabilities. As lava cools, it shrinks, generating stress in the material. This stress is relieved if the lava cracks at regular intervals [24]. This is the mechanism underlying

the formation of hexagonal columnar jointings and similar structures in drying corn starch cakes. While hexagons have been observed in these planar surfaces, and radial cracks have been observed in a circular anulus [64], the crack structure occuring in drying cylinders remains unknown. Our preliminary work on drying corn starch suggests that lateral flat cuts as observed in wombat feces is one possibility, and may account for the remaining two faces of the cube.

The significance of cubic feces in evolution also is ripe for future work, and we suggest some potential directions here. It is well known that wombats deposit aggregations of feces on prominent surfaces, such as rocks or logs, as exemplified in **Figure 3.1b**, and it is widely hypothesized that their cubic shape facilitates the feces remaining on the surface. In preliminary tests, we explore the ability of cubic feces to prevent rolling and bouncing. We form balls of dough in the same shape and size of wombat feces and drop them from a height of 20 cm, comparable to the height of an adult wombat anus. When the feces land on flat surfaces, cubes travel farther than spheres. When dropped onto inclined surfaces of $8°$, cubes end up 20 cm closer to the original impact site than spheres on average. Similar such tests could easily be done with natural substrates.

It is possible that the feces cubic shape increases the surface area so that it can facilitate olfactory communication. Elevated scent-marking is a common behavior in many mammals and is hypothesized to increase scent dispersal and visibility [65] [66]. The purpose of scent-marking is typically territorial [66] [67], however there is evidence that feces are also used in social communication [68] or communicating reproductive status [69].

3.4   Materials and Methods

Wombats are all obtained from humanely euthanized individuals that were the victim of vehicle collisions. In this study, we present data from 3 wombat dissections. All dissections are performed after the specimen is frozen and thawed one time. In 2018, we dissect a young female wombat (2-3 years old). In 2019, we dissect an adult male wombat ($>$ 2

years old). And in 2020, we dissect a young male wombat (< 2 years old).

3.4.1   Histology

We perform E&H staining on tissue samples taken every 1 cm along the entire circumference of both the proximal and distal colons. This sampling and staining was performed 3 times for both the proximal and distal colons at locations separated by 1 cm axially in their respective regions. Sections were cut at between 14 and 19 microns. The staining allows for the visual identification of the four major tissue layers: mucosa, glandular layer, circular muscle, and longitudinal muscle. We measured the thickness of each layer underneath a microscope using NIS-Elements software.

3.4.2   Dryness testing

We evaluate fecal water content in the lower proximal colon (2 - 2.5 m from the anus) and distal colon (0 - 0.5 m from the anus). Five representative pieces of fecal material are extracted from the distal colon (all pieces are formed and distinct cubes) and two from the proximal colon (pieces not distinct, derived from the continuous slurry),they are weighed, dried at $60°$C until they no longer changed in mass (96 hours) and then re-weighed.

3.4.3   Tensile testing

The cut is made at a 50 cm distance from the anus. To measure the local stiffness at different azimuthal locations, we laser-cut a stencil to draw tick marks every 4 mm along the circumference of a 5 cm long tissue sample of proximal and distal colon. A ZXUEZHENG surgical marker (0.5mm, from Amazon) provides the most visible tick marks. Two such rows are drawn 1 cm apart on each sample. To perform the tensile test, the sample is cut longitudinally.

Both ends of the cut tissue are clamped down with custom-made clamps (See **Figure 3.3e**). Each clamp is made from laser-cut acrylic with sandpaper hot-glued to the

inside, preventing the tissue from slipping. From one clamp, the sample is hung off a rod, while the bottom of a disposable water bottle is hung off of the bottom clamp. The sample is stretched by adding increments of water to the bottle. The clamp and bottle weigh 51.6 g. The sample is stretched by adding water to the bottle, a total of 7 times, in 25 ml increments. The sample is allowed to settle before the next increment of water is added. The test is recorded and we use the `video labeler` app from the Computer Vision toolbox in MATLAB to track the location of the interior end of the left row of tick marks. To get a full $360°$ test of the sample, 2 adjacent samples are prepared and the longitudinal cut is performed $180°$ offset of the other, allowing us to test regions of the tissue that would otherwise be covered by the clamps.

As shown in **Figure 3.3f**, the first sample is denoted by blue dots while the other is denoted by red diamonds. The black line shows an averaging between the two samples at that azimuthal location, ignoring the edge-most data points of both samples due to edge effects from clamping down on the tissue.

3.4.4   Solving the equilibrium model

The intestine simulation does not attempt to model the non-Newtonian nature of the feces itself. Instead it represents the feces phenomenologically as increased damping and mass, aggregated at the intestinal walls. Without the feces, the nodes may take on conformations that allow the springs to cross themselves in 2D space, which is not physically possible in the biological system. We find that using the equilibrium solution as the initial state helps prevent intersection of nodes during the contraction simulation.

The wombat intestines are modeled by a ring of springs (See **Figure 3.4a**). The equilibrium shape is described by the length of the springs in the soft region l_A, the length of the springs in the stiff region l_B, the angles between the springs in the soft and stiff regions, ϕ_A and ϕ_B respectively, and the angle at the interfacial nodes between the stiff and soft regions ϕ_{AB}. A constant pressure, P, is exerted outwards on the nodes until the springs

come to an equilibrium length. To solve for 5 unknown values, we require a system of 5 equations. Four of the equations come from local force balances: parallel to the angular bisector in the soft region (See Equation Equation 3.5 and **Figure 3.4b**) and the stiff region (See Equation Equation 3.6), and for the interfacial node, both parallel and perpendicular to the angular bisector (See Equations Equation 3.7 and Equation 3.8). The equilibrium shape forms a convex $4n$-gon requiring the summation of the angles to be $\pi(4n - 2)$ (See Equation Equation 3.9).

$$\tan(\phi_A/2) = \frac{8nk(l_A - l_0)}{Pl_A} \tag{3.5}$$

$$\tan(\phi_B/2) = \frac{8Cnk(l_B - l_0)}{Pl_B} \tag{3.6}$$

$$\tan(\phi_{AB}/2) = \frac{8nk(l_A + Cl_B - (C + 1)l_0)}{P(l_A + l_B)} \tag{3.7}$$

$$\tan(\phi_{AB}/2) = \frac{P(l_B - l_A)}{8nk(l_A - Cl_B + (C - 1)l_0)} \tag{3.8}$$

$$\pi(4n - 2) = 2(n - 1)(\phi_A + \phi_B) + 4\phi_{AB} \tag{3.9}$$

In equations Equation 3.5-Equation 3.9, n is the number of nodes in each of the 4 sections of the ring, l_0 is the resting spring length, k is the base spring stiffness, and C is spring stiffness ratio between the stiff and soft regions.

The equilibrium shape is numerically calculated using the MATLAB function `fsolve`. Both options `MaxIterations` and `MaxFunctionEvaluations` are set to 10^8. Each of the 4 regions are composed of $n = 50$ nodes as increasing n greater than 50 did not seem to change the resulting shape. The following are the parameters used in the default simulation. The unstretched length of every spring is $l_0 = 2\sin\left(\frac{\pi}{4n}\right)$, resulting in an unstretched ring of radius $R_0 = 1$ cm, matching the unstretched radius of the wom-

bat's distal colon. The base spring stiffness is $k = 0.1 \ 10^4$g/sec^2, and the stiffness of each spring was $4nk$ and $4Cnk$ for the soft and stiff springs respectively. The spring stiffness ratio is $C = 4$. Multiplying the spring stiffness by $4n$ normalizes the overall stiffness of the ring to be independent of the number of nodes used in the simulation and results in the softer spring stiffness to be equivalent to 0.2 N/mm as found from tensile testing. The function fsolve requires an initial guess at the solution, $(l_A, l_B, \phi_A, \phi_B, \phi_{AB}) = (l_0 + 10^{-4}, l_0, (4n - 2)\pi/(4n), (4n - 2)\pi/(4n), (4n - 2)\pi/(4n))$.

The simulation fails to run if the equilibrium solution cannot be found. This may happen when the spring stiffness ratio C is too close to 1. When $C = 1$ the system is overconstrained and, as described to the MATLAB function fsolve, cannot find the equilibrium solution. We find this happens when $C < 2$. MATLAB may also fail to find the equilibrium solution if k is too high. This may be due to Equations Equation 3.5-Equation 3.8 holding too much weight, not allowing fsolve to find a solution that also satisfies Equation Equation 3.9. Due to this constraint, we measure all masses in units of 10^4g, to keep $k < 1$.

3.4.5 Simulating the model intestine contractions

The contraction is simulated by solving the equations of motion according to Newton's Second Law, $F = ma$, **Equation 3.10**. Each node is subject to two neighboring spring forces and a damping force.

$$m\dot{\vec{v}}_i = k_i(||\vec{x}_{i+1} - \vec{x}_i|| - l_0)(\widehat{x_{i+1} - x_i}) + k_{i-1}(||\vec{x}_{i-1} - \vec{x}_i|| - l_0)(\widehat{x_{i-1} - x_i}) - b\vec{v}_i. \quad (3.10)$$

where $||\vec{u}||$ indicates the magnitude of vector u and $\hat{u}$ means that vector u is scaled to be a unit vector. We close the system with the definition of velocity,

$$\vec{v}_i = \dot{\vec{x}}_i \qquad (3.11)$$

The differential equation is solved over a time period of $t = [0, 40$ sec] using the MAT-

LAB function `ode45`. For simulations involving changes in damping, the simulation time is extended linearly as viscosity was increased, according to $t_f = 10^5 b$, where t_f is the duration of the simulation, and b is the damping coefficient. The equilibrium solution is used to get the initial xy coordinates of all $4n$ nodes and their initial velocities are set to 0.

The following are the parameters for the default simulation. The added mass of each node is set to $m = 4.5 \times 10^{-6}$ 10^4g. This mass is calculated by multiplying our 2D density of feces, $\rho_{2D} = 1$ g/cm^2 by the equilibrium mean radius squared, R^2, then dividing by the number of nodes. Recall that mass must be measured in units of 10^4g to keep the base spring stiffness k low. The damping coefficient is set to be $b = 4.5 \times 10^{-3}$ 10^4g/sec . To contract the system, the rest length of the springs is decreased, from l_0 to $l_0/4$. The system oscillates as a square wave between l_0 and $l_0/4$ with a period $\tau = 1$ sec. Over the simulation time, this period results in 40 simulated oscillations and Re=10^{-3}.

3.4.6   Calculating curvature

The shape of the simulation is analyzed by calculating the curvature at 20 azimuthal positions. Nodes from the simulation are translated so that the center is located at $(0, 0)$. They are then binned together according to their θ location in polar coordinates. While in polar coordinates, the points are rotated so that the center of the bin is at $\theta = \pi/2$. The points are mapped backed to Cartesian coordinates so that we may fit a degree 2 polynomial $y = f(x)$ to the points. From the polynomial, the average curvature of those points is calculated according to **Equation 3.12**.

$$\kappa_{avg} = \frac{1}{x_{max} - x_{min}} \int_{x_{min}}^{x_{max}} \frac{f''(x)dx}{(1 + f'(x)^2)^{3/2}} = \frac{1}{x_{max} - x_{min}} \left| \frac{f'(x_{max})}{\sqrt{1 + f'(x_{max})^2}} - \frac{f'(x_{min})}{\sqrt{1 + f'(x_{min})^2}} \right|$$
$$(3.12)$$

3.4.7 Quantifying Squareness

The wombat feces themselves are not perfect cubes, as the corners, while distinct, are clearly rounded. There exist several metrics for measuring a shape's roundness [60]. For measuring squareness, we found a single existing metric called the squircle [61]. Attempts to use it on our biological data showed that it was not robust to noise. We propose a new metric to evaluate squareness S which comes from comparing the measured curvature $\kappa(\theta)$ to a reference curvature signal.

When considering the reference curvature signal, note that a circle displays constant curvature for all values of θ, while a square has $\kappa(\theta) = 0$ for all values of θ except $\kappa(\theta) = \infty$ at each of the 4 corners. The template for our reference signal is then based upon the following impulse function

$$f_\lambda(x) = \frac{1}{\lambda} e^{-|x|/\lambda}. \tag{3.13}$$

We can check the validity of this equation by considering the limit as λ tends to infinity: $\lim_{\lambda \to \infty} f_\lambda(x)$ =constant, behavior which is similar to the curvature signal of a circle. Likewise, for the limit as λ tends to zero, $\lim_{\lambda \to 0} f_\lambda(0) = \infty$ and $f_\lambda(x|x \neq 0) = 0$, similar to the curvature signal around a single corner of a square. We will use λ to describe the sharpness of a shape's corners. This impulse function also has the added benefit that the area under the curve is constant for all λ.

$$\int_{-\infty}^{\infty} \frac{1}{\lambda} e^{-|x|/\lambda} \mathrm{d}x = 2 \tag{3.14}$$

We use this property to scale the function based on the size of the shape. For a circle with area A

$$\kappa_{circle}(\theta) = \sqrt{\frac{\pi}{A}} \qquad \int_0^{2\pi} \kappa_{circle}(\theta)\mathrm{d}\theta = 2\pi\sqrt{\frac{\pi}{A}}. \tag{3.15}$$

We may then scale our reference curvature signal for any arbitrary shape such that the area under the curve is $2\sqrt{\frac{\pi^3}{A}}$.

To match the 4 peaks in curvature that a square displays, we express the curvature as a piece-wise function, mapping the original infinite domain to a finite one. In doing so, our function's area under the curve is no longer conserved over λ. We remedy this by scaling by the integrated area under the curve, from zero to $\pi/2$, which is relevant for each of the pieces of the piecewise function. Overall we have

$$\kappa_{ref}(\theta, \lambda) = \frac{\sqrt{\frac{\pi^3}{A}}\left(\frac{1}{\lambda}e^{-|\tan(\theta-\psi)/\lambda|}\right)}{\int_0^{\pi/2}\frac{1}{\lambda}e^{-\tan\tilde{\theta}}d\tilde{\theta}} \tag{3.16}$$

where

$$\psi = \begin{cases} \pi/4 & \theta \in (0, \pi/2) \\ 3\pi/4 & \theta \in (\pi/2, \pi) \\ 5\pi/4 & \theta \in (\pi, 3\pi/2) \\ 7\pi/4 & \theta \in (3\pi/2, 2\pi) \end{cases}$$

The reference function displays discontinuities at $\theta = \frac{n\pi}{2}$, $\forall n \in \mathbb{Z}$. From κ_{ref}, we inherently get the first component of our squareness metric in λ, in which high values of λ indicate the shape is very circular, while values close to 0 indicate the shape is square.

To match the measured $\kappa(\theta)$ to the proper value of λ, we cross-correlate the signals $\kappa(\theta)$ and $\kappa_{ref}(\theta, \lambda)$ using the `xcorr` function available in MATLAB (See **Figure 3.5a**). Both signals must be sampled at the same values of θ. The measured $\kappa(\theta)$ is made continuous by linearly interpolating between values. The function `xcorr` finds the correlation between signals at varying lags, rotating the shape until the curvature signals are aligned. When performing the cross-correlation, we input 3 periods of each curvature signal, $\theta = [0, 6\pi]$ and specify that the lag may not be more than 2π. This prevents `xcorr` from correlating to different signals by only comparing a small part of each signal. We numerically find the value of λ that yields the maximum correlation x using MATLAB's built-in `fminsearch` and an initial guess of $\lambda = 1$. With the optimal value for λ and the corresponding correlation

51

x, we calculate squareness as

$$S = x^{10}(1 - 2\arctan(\lambda)/\pi). \qquad (3.17)$$

The range of S is $(0, 1)$ where $S = 1$ indicates that the shape is perfectly square, and $S = 0$ indicates that the shape is either perfectly circular or very much not square. The correlation, x, is raised to the 10th power. This exponent weights the correlation to ensure that the shape is given a high score only when it has 4 peaks in curvature rather than just 2 very high peaks in curvature. In practice, 2 high peaks in curvature may result in a correlation of $x \approx 0.9$. Raising the correlation to the 10th power sufficiently punishes these non-square shapes.

We illustrate the evaluation of squareness with a numerical example. Consider a single frame at $t = 7.9$ sec from the square simulation using the default parameters listed above ($C = 4$, $m = 4.5 \times 10^{-6}$ 10^4g, $b = 4.5 \times 10^{-3}$ 10^4g/sec).The function `ode45` gives the xy coordinates of all n nodes at each time point. From these coordinates, we calculate curvature κ using equation Equation 3.12 for each bin of nodes. We then get a function $\kappa(\theta)$ for any arbitrary value of θ by linearly interpolating between calculated curvature values. We sample the curvature $\kappa(\theta)$ every $0.6°$ (0.1 radians) from $0.6°$ to $359.4°$. The resulting vector of curvature values is then repeated 3 times so that cross-correlation by the function `xcorr` will not be inflated by comparing too few data points. Using the function `fminsearch` we compare the curvature $\kappa(\theta)$ to the reference curvature $\kappa_{ref}(\theta, \lambda)$ as described by Equation Equation 3.16, sampling at the same values of θ, searching for the value of λ that yields the highest cross-correlation. For $t = 7.9$ sec, this optimal value is $\lambda = 1.5$ with a cross-correlation of $x = 0.98$. **Figure 3.5a** shows the curvature from the simulation (solid black line) as well as the reference curvature $\kappa_{ref}(\theta, \lambda = 1.5)$ (dotted blue line). The range of λ is $(0, \infty)$, so we map λ to a range $(0, 1)$ with 1 indicating highest squareness and multiply it with the cross-correlation value x^{10} as in Equation Equation 3.17. The resulting mapping, from **Equation 3.17** yields a squareness of $S = 0.3$. We repeat this procedure for every

time increment in the contraction.

3.5 Ethics

For the CT-scanning, Animal Ethics approval was sought and granted by the Taronga Conservation Society Australia (protocol number 3e0419).

PELLET FECES FORMATION THROUGH DRYING AND CRACKING

4.1 Introduction

The goal of this study is to provide a physical argument for the length of pelleted feces. While many animals have been known to generate these feces, the mechanisms responsible for this length are still to be understood. Understanding how feces length is caused may provide input into how an animal's digestive health is evaluated based on the form of their feces.
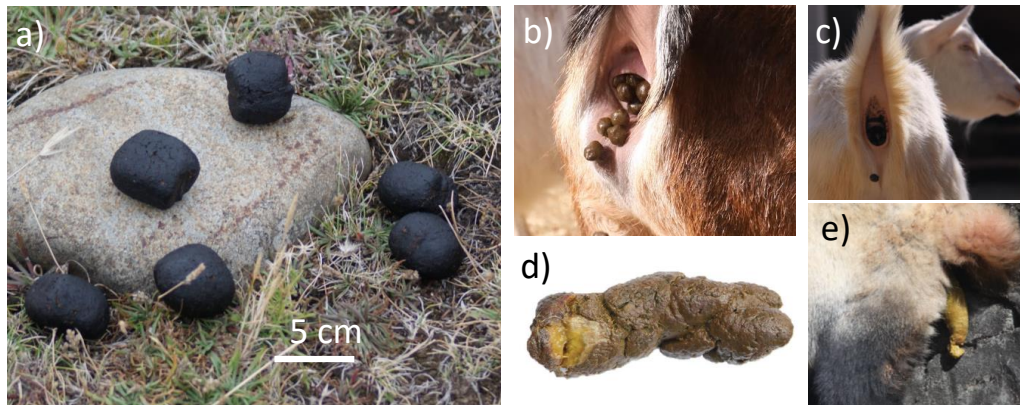
Figure 4.1: Feces geometries. (a) The bare-nosed wombat forms cubic feces. Pelleted feces from (b) a Nubian goat and (c) a Nigerian dwarf goat. Cylindrical feces from (d) a dog and (e) a panda.

We propose that this length is set by material breaking up within the intestines due to drying. As food is digested, the intestines absorb moisture out of the material. This hypothesis is inspired by a geophysics phenomenon known as columnar jointing. To support this hypothesis, we present allometric relationships for the size of pelleted feces, and scaling relationships for the water flux. We compare these results to analogous results for columnar jointings.

Columnar jointing is typically seen in cooling lava beds. The lava does not cool homogeneously, but rather a cool layer forms atop the deeper warm layer. As the cool layer loses heat, it contracts but the warm layer beneath stays the same volume. This mismatch in volumes leads to shear strain in the cool outer layer which is relieved by a regular pattern of cracks. Columnar jointing is not just caused by a loss of heat, but has been shown to happen due to a loss of moisture in porous media. In this way, the polygonal cracking patterns of columnar jointing can be found everywhere, from drying paint to the surface of Mars[25].

The formation of a dry outer layer and a wet inner layer is due to the physics of diffusion of water through porous media. To understand how this process occurs in an intestine, we first review how it occurs in a planar structure. Drying creates non-homogeneity in the media, in which a dry outer layer contracts against an inner wet layer. These layers are created by a concentration-dependent diffusivity $D(c)$ where c is the local water concentration. At high water concentration, liquid water fills the pores, so diffusion transport of molecules occurs in this liquid state. In this regime, diffusion decreases with decreasing concentration as shown in **Figure 4.2b**. As the water concentration decreases, liquid no longer spans all of the pores, and the molecules diffuse as vapor. In this regime, diffusion increases with decreasing concentration [70]. At a critical water concentration between these two regimes, c_m, diffusivity is at a minimum D_m. This minimum diffusivity D_m maintains a sharp transition between the dry outer layer in the vapor transport regime, and the wet inner layer in the liquid transport regime.

Both the flux of moisture and heat out of a material causes the material to shrink, which builds up the strain energy to cause cracks. Often moisture experiments have been used to simulate the behavior of lava cooling. An inverse relationship between the flux of moisture and the distance between cracks, has first been shown empirically [71], and then reaffirmed through dimensional analysis [24]. This inverse relationship is based on the difference in moisture of the dry outer layer and the wet inner layer. Diffusion naturally redistributes

the moisture to be more uniformly concentrated. High differences between the dry and wet layers are then only achieved if the water leaves the system at a sufficiently high rate as to overcome diffusion. The difference in moisture between layers leads to stress in the dry layer as it strains to contract during drying, while the wet layer maintains its size. Cracking relieves this stress. If more stress builds up in the dry layer due to high rates of moisture flux, more cracks form, causing the cracks to be closely spaced together. Therefore, in the feces, we expect that higher flux of water out of the feces leads to closely spaced cracks, which leads to pellets of shorter length.
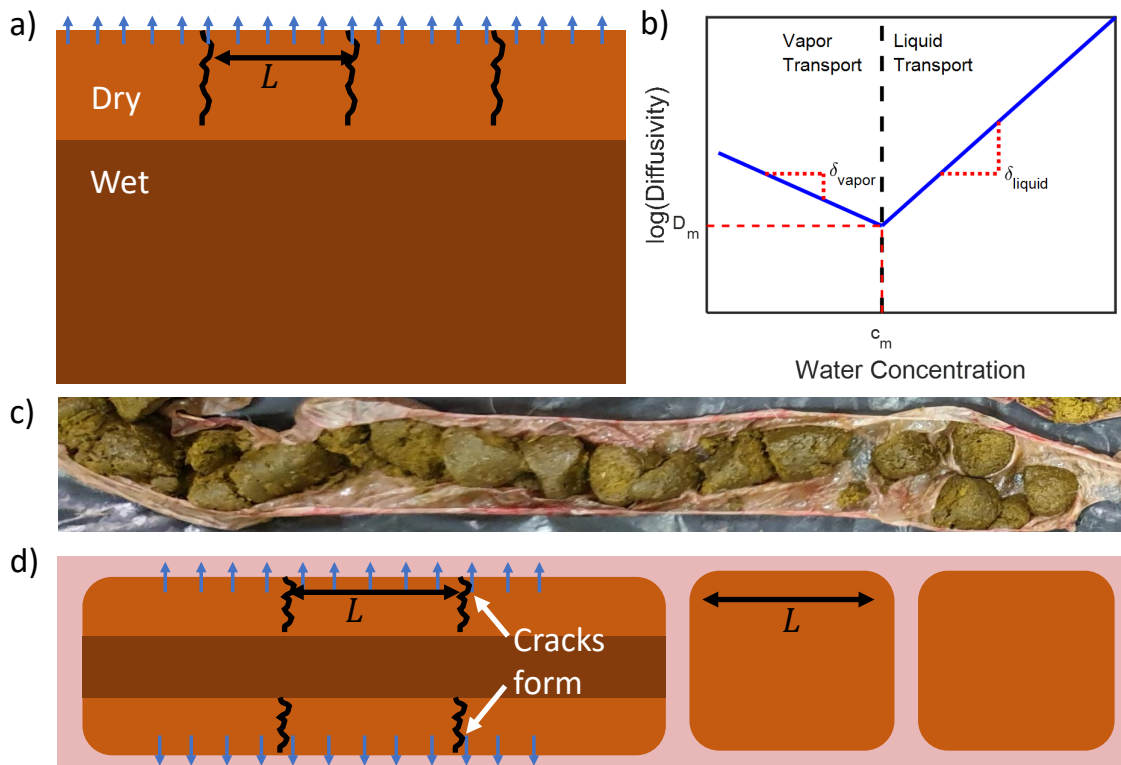
Figure 4.2: We hypothesize that drying leads to pellets forming in the intestines. (a) As porous media dries, it forms a dry surface layer and a wet lower layer. Regular patterns of cracks form in the dry layer. (b) These distinct layers are facilitated by a water concentration dependent diffusivity, in which the minimal diffusivity is found in the transition between the wet and dry layers. (c) A similar regular break-up of feces is observed in wombat intestines. (d) We hypothesize that as water is removed from the feces, a dry layer forms with a wet inner core, leading to cracking into pellets.

In this study we consider water content trends among mammalian feces. These results

are presented in section 2. In section 3, we discuss the implications and how these results fit in with other research. A detailed description of our methods are in section 4.

4.2 Results

4.2.1 Feces shape and water content

We begin with the hypothesis that pellet feces are drier than cylindrical feces. We collect the fecal water content across 22 terrestrial mammal species found in physiology studies [72, 73, 74, 75, 76, 77, 78, 79, 80, 81, 82, 83, 84, 85, 86, 87, 88, 89, 59, 90, 91]. We took the water content value from the control group that did not receive any experimental intervention of each study. For the warthog and wombat, we measured the water content directly. Water content is measured by weighing the sample to find m_{wet}, then baking the sample to dehydrate it, and re-weighing it again to find m_{dry}.

$$w = \frac{m_{wet} - w_{dry}}{m_{wet}} \tag{4.1}$$

We subjectively characterized each feces as pellet, cylinder, or cow pie based on images of the feces from the literature.

Figure Figure 4.3a shows the water content of mammalian feces, arranged from lowest to highest water content. The resulting arrangement shows support for our hypothesis in which pellets (the red columns) have water content $w < 0.65$ and cylinders (the black columns) have $w > 0.65$. Pellet-forming animals include various mice, rats, moles, antelope and goats. Generally larger animals such as monkeys, warthogs, horses, wallaroos and humans have cylindrical feces. Note that the very wettest fecal states, such as the cow pie, are up to 90 percent water and thus do not have enough solid matter to form either pellets or cylinders.

In dissecting a wombat's intestines, feces removed from the intestine also follows this classification of cylinders being wet and pellets being dry. Feces found at the end of the

proximal colon have the shape of large cylinders and water content of 0.80, while feces found in the distal colon have the shape of pellets and water content of 0.54.

4.2.2 Flux Scaling

According to our columnar jointing hypothesis, the spacing of the cracks in feces would be inversely proportional to the flux of water into the intestines. This idea is true for two-dimensional planes, in which the length scale of the polygons formed is inversely proportional to the flux of water evaporating from the surface [92, 71]. However, the idea has not yet been tested in one-dimensional settings similar to that of intestines.

In order to show that the process of feces pellet generation is similar to that of columnar jointing, we use previous literature measurements to derive a scaling law for the average flux J of water through the intestinal wall. To maintain equilibrium, we require that all water intake is either absorbed through the intestines or excreted in feces. This relationship can be written:

$$\dot{m}_{w,in} = \dot{m}_{intestine} + \dot{m}_{w,out} \tag{4.2}$$

where $\dot{m}_{w,in}$ is the water intake, $\dot{m}_{intestine}$ is the water flux through intestinal walls, and $\dot{m}_{w,out}$ is the water ejected through feces. Note that the water flux through the intestinal wall can then be ejected through the body through urine, sweat, or evaporation, but tracking that pathway is not necessary to understand feces shape.

The water intake $\dot{m}_{w,in} = \dot{m}_{in} - \dot{m}_{dry}$ can be written as the the difference between the total mass intake and the dry mass intake. The total mass intake in (kg/day)[48] is

$$\dot{m}_{in} = 0.097 M^{0.97} \tag{4.3}$$

where from hereon, M is body mass (kg). The dry mass intake (kg/day) [93] was found to be

$$\dot{m}_{dry} = 0.0004 M^{0.75}. \tag{4.4}$$

The excreted water $\dot{m}_{w,out} = w\dot{m}_{out}$ may be written as the product of the water content and the defecation rate. We start with the rate at which they excrete feces (kg/day) [48]

$$\dot{m}_{out} = 0.01M^{0.83}. \tag{4.5}$$

Based on our literature search, it does not seem that water content scales with mass, so we use 0.65 as a conservative maximum water content for pelleted feces.

The water flux $J = \dot{m}_{intestine}/A$ may be written as the ratio of $\dot{m}_{intestine}$ and the surface area $A = \pi L_{colon} D_{colon}$ of the intestinal wall, where the colon is the shape of a cylinder. We only consider the colon because this is where the feces goes from a watery content to its final shape, as shown in **Figure 4.2c**. The length (cm) and diameter (cm) of the colon [48], which are given by

$$L_{colon} = 28M^{0.71} \tag{4.6}$$

and

$$D_{colon} = 0.83M^{0.36}. \tag{4.7}$$

In all, we can write

$$J = \frac{\dot{m}_{in} - \dot{m}_{dry} - w\dot{m}_{out}}{\pi L_{colon} D_{colon}} \tag{4.8}$$

where we have defined each of the terms.

This gives a scaling of flux as $J \sim M^{-0.12}$. If columnar jointing is the mechanism that cracks the feces, we would expect $L \sim J^{-1}$. According to a scat recognition field guide, among mammals that form pelleted feces in North America, the pellet length scales with animal body mass M according to $L \sim M^{0.17}$, $R^2 = 0.69$, very similar to the inverse of the flux scaling (See **Figure 4.3b**) [94]. [24, 71].
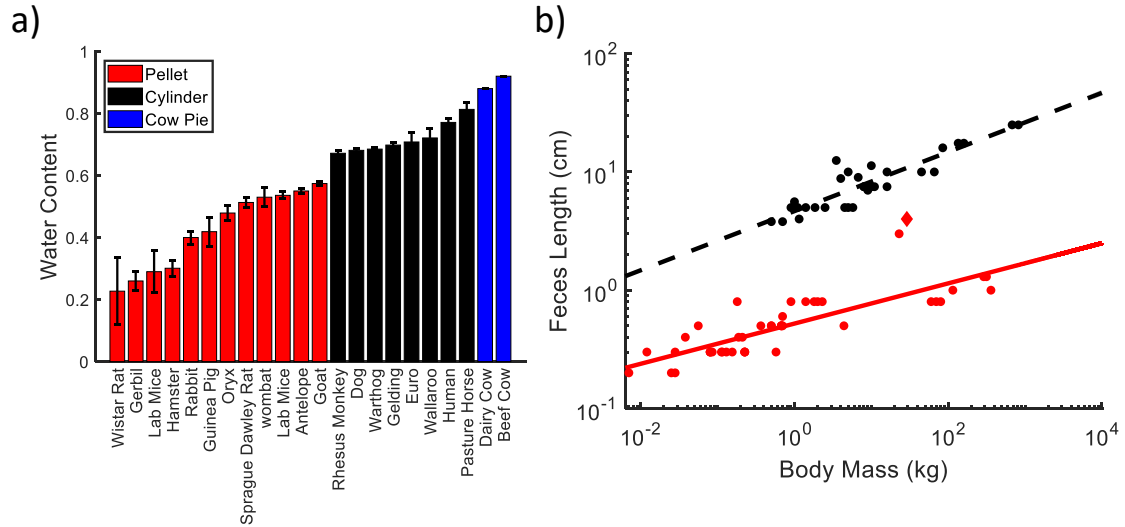
Figure 4.3: Pellet data collected from literature search. (a) Pellets are drier than other feces, having a water content less than 0.65. (b) The length of the pellet tends to increase with the size of the mammal according to the scaling $L \sim M^{0.17}$

4.3 Discussion

In this study, we provide evidence that feces break up within the intestine due to the removal of moisture during digestion and that this process is similar to that of columnar jointing. Break up into pellets occurs when the water content drops below 0.65. Above this water content, feces maintains a elongated cylindrical shape, suggesting that no dry outer layer forms within the feces. Based upon past drying research, the leads to a prediction for future investigation. The diffusivity of water within feces must have a minimal diffusivity when the water content is 0.65. That is to say, the system transitions between a liquid transport regime to a vapor transport regime at a water content of 0.65.

Our observation that pelleted feces form when the water content is below 0.65 is further supported when compared to studies of human feces. The Bristol Stool Chart maps qualitative descriptions of human feces to quantitative values from 1-7, with 1 indicating constipation and 7 indicating diarrhea. Of note, a Bristol number of 1 describes the feces as hard nuts that are difficult to pass. The physical description of the feces is similar to that

of pelleted feces. In fact, feces characterized as a Bristol number 1 had a water content of 0.65, very similar to the threshold water content for pelleted feces found in this study, and much lower than a typical water content of 0.80 [95].

Future work and applications may focus on the appearance of pelleted feces during human constipation. It is intriguing that pelleted feces are normal for some animals, but are difficult to expel for humans. Aquaporins, a family of proteins that play an active role in removing water from feces during digestions, also seem to add water back to the feces[96]. Future comparative studies could investigate the evolutionary trade-offs of pelleted feces as well as adaptations allowing for pelleted feces to be dispelled. By understanding how pelleted feces form, we may gain a better understanding of how to prevent and treat human constipation.

Our flux scaling along with observed pellet length scaling continue to support the hypothesis that columnar jointing leads to pellet formation. Prior columnar jointing work finds that the flux is inversely proportional to the spacing between cracks. Similarly, we find that the scaling of flux with respect to body mass have approximately inverse powers. Using body mass as an intermediate variable as we have done has its downsides because it does not capture outliers among the scaling laws. The pellet length scaling comes from only North American mammals. Meanwhile, the Australian bare-nosed wombat has feces of length 4 cm, longer than most pelleted feces used to calculate the scaling law. The wombat also has an exceptionally long colon, causing the flux to be much lower that that of most mammals, potentially explaining the exceptionally long feces, but also illustrating the need for one-to-one measurements of pellet length and water flux to more strongly establish the trends found here.

This work provides evidence that columnar jointing leads to pelleted feces within the intestines. Specifically, this explains how feces break up within the intestine of the wombat, which in combination with prior work, explains how the wombat forms cubic feces.

4.4 Methods

The wombat used in the dissection to get the water content of feces in the proximal and distal colons was obtained from humanely euthanizing an individual that was the victim of a vehicle collision. The wombat was dissected in 2019 and an adult male (> 2 years old).

CHAPTER 5

CONCLUSION

This thesis considers three examples of the interactions between biological shape and its underlying physics. We use a combination of experiments and theoretical models to see both how geometry influences physics and how different forces influence geometry.

Chapter 2 was inspired by the ability of the star-nosed mole to hold onto bubbles much larger than the capillary length. We quantified the stability of the bubble as the angle at which the bubble could be tilted until it was released. Flat discs are poor at stabilizing bubbles. However, bends in the disc or triangular gaps are able to allow bubbles to peek through. These bulges create counterbalance, allowing the disc to be tilted to nearly double the angles of flat discs. We showed that certain gap sizes are optimal, both providing sufficient counterbalance for the bubble, but also preventing the bubble from escaping the gap. This idea of the bubble counter-balancing itself is a novel and simple way to increase a bubble's stability, even if the bubble is of a length-scale much larger than the capillary length. Our study provides one step towards building an underwater sensor based on the use of bubbles to capture odors.

In Chapter 3 we show that wombats form corners in their feces using intestinal contractions coupled with the unique non-uniform material properties of their intestines. The questions of how and why wombats form cubic feces make up a compelling case study of the intersections between physiological, behavioral, and evolutionary ecology. However, they also have value in a range of other fields, particularly as a novel method of cube formation in manufacturing, and may also provide some clinical pathology insight for certain human illnesses changing the tensile properties of the intestinal tract.

In Chapter 4 we consider how drying leads to feces breaking up into pellets. That pelleted feces are always drier than cylindrical feces suggests that pellets form due to some

drying phenomenon. We believe this phenomenon is similar to the geophysics phenomenon of columnar jointing, however the evidence in support or against this hypothesis is still unclear. Understanding this pellet-formation mechanism could have implications for the comparative evolution of the colon.

This thesis uses simple table-top experiments supported by mathematical modeling to understand the relationship between shapes and physics. These easy experiments allow us to ground our research in reality, providing simple proofs-of-concept. The mathematical modeling allows for more extensive investigation of the phenomena at play and allows us to quantify the contributions made by the mechanisms that we find. This strategy has shown itself to be an efficient approach to understanding nature.

This framework allows reality and mathematics to progress together in which experiments show evidence of a phenomenon while the mathematics allow us to investigate the mechanisms in more detail. This mutual relationship makes feasible contributions from undergraduate students as well as international collaborators. We review how this strategy manifests itself with each project in turn.

The bubble-stability project started with video recordings of myself blowing bubbles in the lab with a boba straw, with the end cut into flaps and folded flat to form a star. I had noticed that the bubble peaked through the gaps of the star and that it seemed more stable to waving around the end of the straw. This led to the tilting experiments and our small gap theory.

This strategy of simple experiments supported by theory had limitations though when we expanded to bubble-sniffing dynamics. We experienced difficulties in designing stripped-down experiments of sucking bubbles back into the apparatus and the various geometries that the bubble took as it was blown out and sucked back in made theory prohibitive.

The wombat feces project started when one of my students inflated balloon inside wombat intestines from our Australian collaborators and noticed some regions stretched more than others. This led to my students developing a fabric wombat intestine mimic with two

stiff regions. This also led to histologies by our collaborators and my students designing tools to send our collaborators to perform tensile testing on fresh wombat intestine. The fabric mimic still presented the problem of getting 4 periods of curvature from 2 periods of stiffness. It was my student' idea that the intestinal contractions might create 2 additional corners. To demonstrate this, they sewed tabs to the outside of the mimic, allowing them to sinch the fabric mimic tight around viscoplastic floam inside the mimic. It did form 4 corners in the floam, but their demonstration was difficult to replicate. This did however inspire my development of the numerical model of contracting springs, used to show the role of inertia in forming corners in the soft regions of the intestine.

These projects, while simple, lead to many new lines of inquiry. In focusing on the mechanics, how these phenomena relate to the biology remains unanswered. The strange abilities of these animals gives inspiration to new technology as well. We proceed to consider both avenues of future work.

While we investigated the mechanisms for how bubbles may be stabilized and how various fecal geometries arise, the biological contexts in which these mechanisms come about still remains unexplored. It is still unknown what leads to the development of 22 appendages growing out of the star-nosed mole's nostrils or what leads to the two peaks in muscle thickness found in the wombat's intestines. The evolutionary motivation of forming cubic feces similarly remains a mystery, as well as the explanation for why some mammals form pelleted feces while others form cylinders. Given the similarity between human feces during constipation and pelleted feces, this last question may actually provide further understanding of human constipation.

These mechanisms provide potential solutions in technology. Machine olfaction is ineffective underwater, yet the star-nosed mole demonstrates how to use olfaction underwater. While the mammalian olfactory system is similarly sensitive to contact with water, the star-nosed mole uses bubbles as an interface between its sensory system and the environment. While we have extensive technology for detecting explosives, none of it is currently used

to find underwater unexploded ordinance. By understanding how to stabilize the bubble during underwater sniffing, we may imitate the star-nosed mole's behavior and sniff for such ordinance.

The wombat intestines provide a potentially new way to manufacture cubes in soft material. Such a technique may find future application in producing cubic fruit. By growing the fruit within a mimic intestine, peristaltic contractions may massage the fruits to encourage growth into a square cross-section.

Nature is a source of inspiration in a number of fields from chemistry to material science. In this thesis, it is a source of inspiration for capillarity and soft matter. We see how forces alter the shapes of bubbles and feces, allowing them to perform unorthodox functions.

Appendices

Journal Papers

- Lee, A. B. and D. L. Hu. 2018. "Bubble stabilization by the star-nosed mole." *Physical Review Fluids*, **3**(12).

- Yang, P., A. B. Lee, M. Chan, M. Kowalski, K. Qiu, C. Waid, G. Cervantes, B. Magondu, M. Biagioni, L. Vonelgust, A. Martin, A. Edwards, S. Carver, and D. L. Hu. "Intestines of non-uniform stiffness mold corners into wombat feces." Soft Matter. DOI: 10.1039/d0sm01230k.

- Lee, A. B., B. Magondu, P. J. Yang, G. Cervantes, M. Meng, C. Kaminski, S. Carver, and D. L. Hu. "Drying dynamics of pellet feces is similar to columnar jointing." To be submitted to Integrative and Comparative Biology.

Refereed Conference Papers

- Lee, A. B., T. L. Spencer, J. Pillarisetti, M. Ersted, and D. L. Hu. 2017. "mimicking sniffing for improving machine olfaction". ISOCS/IEEE International Symposium on Olfaction and Electronic Nose. Montreal, Canada.

Textbook

- Weitz, J. S., A. B. Lee, A. S. Zamani, and N. English. Quantitaive Biosciences in Python: Dynamics Across Molecules, Organisms, and Ecosystems. In progress at Princeton University Press.

Invention Disclosure

- Spencer, T. L., A. B. Lee, and D. L. Hu. 2018. Active sensing preconcentrator for improved chemical and particle detection.

Conference Presentations

- Lee, A. B. and D. L. Hu. 2017. "Underwater Sniffing by the star-nosed mole." Division of Fluid Dynamics. Denver, Colorado.

- Lee, A. B., B. Seleb, L. Hanlon, A. Sun, and D. L. Hu. 2018. "Dynamics of bubble-formation by the star-nosed mole." Division of Fluid Dynamics. Atlanta, Georgia.

- Lee, A. B., B. Seleb, L. Hanlon, A. Sun, and D. L. Hu. 2019. "Preventing bubble pinch-off in underwater sniffing." Society for Integrated and Comparative Biology. Tampa, Florida.

- Lee, A. B., P. J. Yang, M. Chan, M. Kowalski, K. Qiu, C. Kaminski, S. Carver, and D. L. Hu. 2019. "Corner formation in the wombat's cubic feces." Division of Fluid Dynamics. Seattle, Washington.

Honors and Awards

- Catalyzing Advocacy for Science Engagement, Georgia Tech representative, 2017

- ISOEN Sniffest Competition, Honorable mention, 2017

- Quantitative Biosciences, Strategic Plan Advisory Group Fellow, 2019

- Ig Nobel Prize in Physics, 2019

Reviewer for Physical Review

- Moreno Soto, A., P. Peñas, G. Jajoinie, D. Lohse, and D. van der Meer. 2020. "Ultrasound-enhanced mass transfer during single-bubble diffusive growth." *Physical Review Fluids*, **5**(6).

APPENDIX B

MIMICKING SNIFFING FOR IMPROVED MACHINE OLFACTION

B.1 Abstract

Sniffing is an important component in mammalian olfaction, serving to draw odors into the nose for detection. Reviewing past studies on animal olfaction, certain aspects such as the sniffing frequency have been found to be common among macrosmotic animals. We compared the airflow velocity, volumetric flow during inspiration, and the cross-sectional area of the nasal cavity for various mammals. We find that bigger animals sniff at a lower frequency and each sniff has a higher airflow velocity. Looking at these aspects of sniffing in more detail and understanding the significance of these common values in animal olfaction informs the design of a pre-concentrator to improve performance in machine olfaction.

B.2 Introduction

Olfaction is a form of chemical sensing meant to provide animals with information about their environment. In machine olfaction, electronic devices are made to "smell" chemicals in the air. This has applications in monitoring pollutants, bomb detection, and noninvasive medical diagnosis[97, 98, 99].

Macrosmatic animals, such as dogs and elephants, rely heavily on olfaction and have an exceptional sense of smell. Humans have employed these animals to a limited extent for bomb detection and medical diagnosis[100, 101]. It is necessary to understand how these animals achieve such a high level of olfaction if we are to replicate and improve upon these systems. Current strategies in machine olfaction typically require steady airflow and temperature modulation [102, 103], but are often slow because they require the system to reach steady state. Work has been done to accelerate the process by engineering transient

features. This includes using sniffing in machine olfaction. When vapors are "sniffed" at 0.08Hz, higher frequency signals can classify acetone and ethanol [104]. By "sniffing" at 5Hz, within the range of animal sniffing behavior, detection of TNT vapors can be improved 16 fold [105].
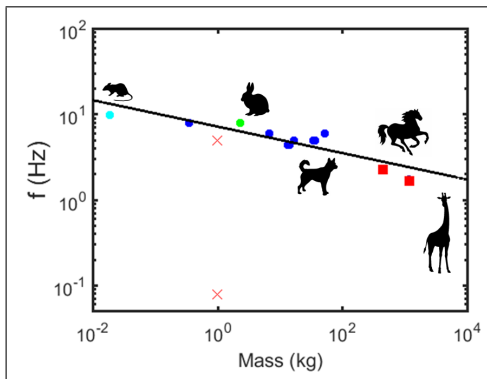
Figure B.1: The sniffing frequency of various mammals were collected from studies (blue [29], cyan [106], and green [107]). We also measured the sniffing frequency of a horse and a giraffe (red squares) from online videos [108][109]. Sniffing frequency appears to have a weak correlation to body mass, $f \sim M^{-0.15}$, $R^2 = 0.78$. We have also plotted two electronic noses that employ sniffing (red x's) [104, 105]

In this review, we compare aspects of olfaction such as the sniffing frequency, volumetric flow, cross-sectional area of the nasal cavity in mammals, and airflow velocity, and consider how this information could help improve uses of sniffing in machine olfaction.

B.3 Methods

The sniffing frequency of various mammals were taken from studies and plotted against their body mass [29, 106, 107]. We also measured a horse's and giraffe's sniffing frequencies from online videos to gain information on larger mammals[108, 109]. For each video, we timed the length of three separate sniffing bouts. We then listened to the audio to manually count the number of sniffs during the bout and calculated the sniffing frequency.

We analyzed the airflow velocity during sniffing by collecting literature values of volumetric flow during sniffs and the cross-sectional area at the olfactory region with respect to body mass [29, 107, 110, 111, 112, 113]. From this data, we could approximate a

power law curve for the airflow velocity with respect to mass according to the following relationship,

$$v = \frac{Q}{A} \tag{1}$$

where v is the airflow velocity, Q is the volumetric flow rate, and A is the cross-sectional area of the nasal cavity (Figure B.2). We then compared airflow velocities within the animals' nasal cavities, by reviewing data from various numerical fluid dynamics models, only considering the olfactory region for this comparison. Values were read from the figures with use of the color scale bars.
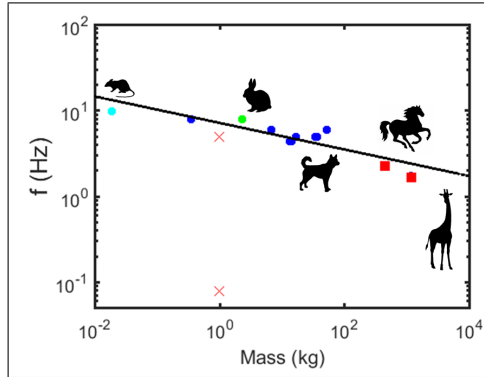
Figure B.2: We collected literature values for the volumetric flow (Q) of sniffs and the cross-sectional area (A) of the nasal cavity at the olfactory region to analyze airflow velocity (v) among mammals.

B.4   Results

Among macrosmatic animals, literature values for sniffing frequency is fairly consistent, between 4-10hz (Figure B.1). However, our measurements of a horse's and a giraffe's sniffing frequency are lower, at 2.3Hz and 1.7Hz respectively. This presents a downward trend with respect to mass, giving a power law curve of

$$f \sim M^{-0.15} \tag{2}$$

where f is the sniffing frequency, M is the mass, and $R^2 = 0.79$.

Among dogs, volumetric flow rate increases with respect to mass according to $Q \sim M^{1.03}$ [29]. With the addition of rats, humans, and rabbits, the power law curve is

$$Q \sim M^{0.92} \tag{3}$$

$R^2 = 0.91$ (Figure B.3). From the literature, we also see that the cross-sectional area also increases with mass

$$A \sim M^{0.73} \tag{4}$$

with $R^2 = 0.63$ (Figure B.4). Then according to equation (1), we approximate the following relationship

$$v \sim M^{0.18} \tag{5}$$

When comparing the airflow velocities in the numerical models, there exists a range of velocities in the olfactory region. Dogs and humans seem to have a much more variable velocity range than rabbits and rats do. With this variation, there seems to be a common subrange from 1-2m/s shared by all of these animals.
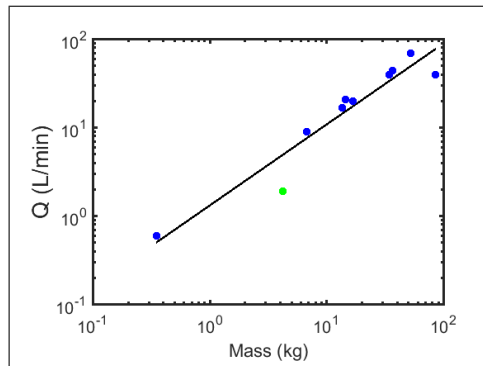
Figure B.3: The volumetric flow during inspiration of sniffs was collected from studies for various breeds of dog, rats, humans (blue markers [29]), and rabbits (green marker [107]). Additional data supports the conclusion that the volumetric flow is a function of mass [29], $Q \sim M^{0.92}$, $R^2 = 0.91$.
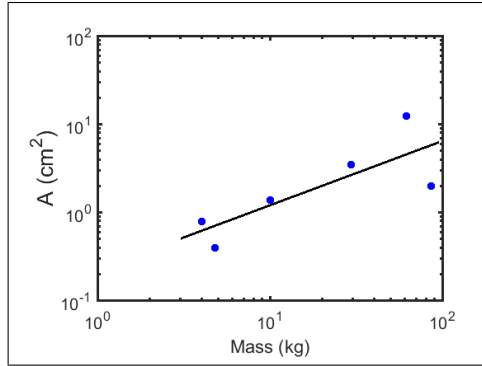
Figure B.4: The cross-sectional area of the nasal cavity at the olfactory region was collected from studies that took MRIs or CT scans of humans, rabbits, dogs, cats, and white-tailed deer [107, 110, 111, 112, 113]. The cross-sectional area is a function of mass, $A \sim M^{0.73}$, $R^2 = 0.63$

B.5 Discussion

From published data, macrosmatic mammals seem to sniff at similar frequencies. It has been suggested that sniffing at this high frequency allows rats to filter out and attenuate background odors [114]. By sniffing at a higher frequency, the animal brings in new air before previously activated olfactory receptor neurons can reset to detect the next set of molecules. This attenuation allows the animal to detect new unique odors more clearly. However, with the addition of our data on horse and giraffe sniffing frequency, it appears as though there is a slight downward trend in sniffing frequency with respect to body mass. This may be due to potential metabolic constraints in how fast the animal can inspire and expire as their size increases. The sniffing frequency appears constant across species because the dependence on body mass is low.

From the volumetric flow during inspiration (Figure B.3) and the cross-sectional area of the nasal cavity (Figure B.4), we conclude that the airflow velocity increases with the animal's body mass, but there is again only a weak dependence on body mass (Figure B.5). In the numerical models, there is turbulent flow for humans and dogs [29, 115], which results in a wide range of velocities in their contour plots. Due to the wide range of velocities for humans and dogs, there is a common subrange of airflow velocities between 1-2m/s for all
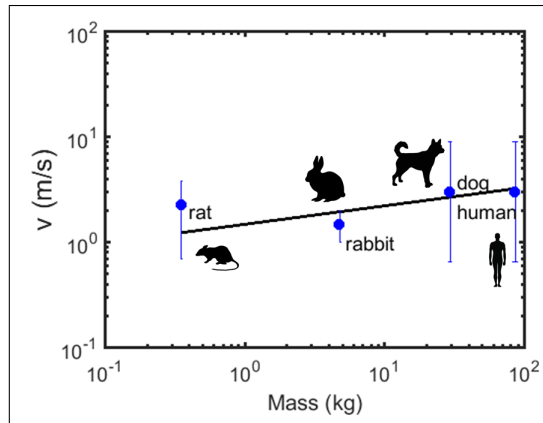
Figure B.5: While the range of airflow velocities in the nasal cavity can be large, every animal has a common sub-range of 1-2m/s. Airflow velocity ranges were read from numerical fluid dynamics models [29, 107, 115]. We approximated a power law curve from the equation $v = \frac{Q}{A}$ where Q is the volumetric flow of a sniff with respect to body mass (Figure B.3), and A is the cross-sectional area of the olfactory region with respect to mass (Figure B.4).

of these animals. This common subrange along with the airflow velocity's low dependence on body mass could suggest an optimal velocity range for interactions between the odors and the receptors.

This data on animal sniffing informs the design of a pre-concentrator for machine olfaction. Using a piston, air can be pulsed in and out at a frequency of 4hz. The air then passes through a valve used to adjust the airflow velocity to 1.5m/s. The resulting signal can be sampled at over twice the sniffing frequency at 10hz. Sniffing will help collect odors on the sensor [105], and DWT will be used to extract features for classification. Such a design could improve transient feature extraction. If in current ongoing experiments, this device proves effective, it will be an important step in employing sniffing for machine olfaction.

B.6 Conclusions

A review of mammalian olfaction shows that the sniffing frequency and resulting airlfow velocity are fairly conserved across species. Further investigation into both of these traits is necessary, but a thorough understanding of their significance in animal olfaction may lead

to important insights in advancing machine olfaction.

REFERENCES

[1] D. W. Thompson, "On growth and form.," *On growth and form.*, 1942, Publisher: Cambridge Univ. Press.

[2] W. J. Bock and G. von Wahlert, "Adaptation and the Form-Function Complex," *Evolution*, vol. 19, no. 3, pp. 269–299, 1965, Publisher: [Society for the Study of Evolution, Wiley].

[3] A. Abzhanov, M. Protas, B. R. Grant, P. R. Grant, and C. J. Tabin, "Bmp4 and Morphological Variation of Beaks in Darwin's Finches," *Science*, vol. 305, no. 5689, pp. 1462–1465, Sep. 2004, Publisher: American Association for the Advancement of Science Section: Report.

[4] S. J. Gould and R. C. Lewontin, "The Spandrels of San Marco and the Panglossian Paradigm: A Critique of the Adaptationist Programme," *Proceedings of the Royal Society of London. Series B, Biological Sciences*, vol. 205, no. 1161, pp. 581–598, 1979.

[5] S. Camazine, "Self-organizing pattern formation on the combs of honey bee colonies," *Behavioral Ecology and Sociobiology*, vol. 28, no. 1, pp. 61–76, Jan. 1991.

[6] P.-G. de Gennes, F. Brochard-Wyart, and D. Quere, *Capillarity and Wetting Phenomena: Drops, Bubbles, Pearls, Waves*. New York: Springer-Verlag, 2004.

[7] J. C. Burton and P. Taborek, "Bifurcation from Bubble to Droplet Behavior in Inviscid Pinch-off," *Physical Review Letters*, vol. 101, no. 21, p. 214 502, Nov. 2008.

[8] J. C. Burton, R. Waldrep, and P. Taborek, "Scaling and Instabilities in Bubble Pinch-Off," *Physical Review Letters*, vol. 94, no. 18, p. 184 502, May 2005.

[9] A. U. Chen, P. K. Notz, and O. A. Basaran, "Computational and Experimental Analysis of Pinch-Off and Scaling," *Physical Review Letters*, vol. 88, no. 17, p. 174 501, Apr. 2002.

[10] D. M. Henderson, W. G. Pritchard, and L. B. Smolka, "On the pinch-off of a pendant drop of viscous fluid," *Physics of Fluids*, vol. 9, no. 11, pp. 3188–3200, Nov. 1997.

[11] H. Tsuge, Y. Tezuka, and M. Mitsudani, "Bubble formation mechanism from downward nozzle — Effect of nozzle shape and operating parameters," *Chemical Engineering Science*, vol. 61, no. 10, pp. 3290–3298, May 2006.

[12] H. Bai and B. G. Thomas, "Bubble formation during horizontal gas injection into downward-flowing liquid," *Metallurgical and Materials Transactions B*, vol. 32, no. 6, pp. 1143–1159, Dec. 2001.

[13] M. H. Jobehdar, K. Siddiqui, A. H. Gadallah, and W. A. Chishty, "Bubble formation process from a novel nozzle design in liquid cross-flow," *International Journal of Heat and Fluid Flow*, vol. 61, pp. 599–609, Oct. 2016.

[14] O. Pamperin and H.-J. Rath, "Influence of buoyancy on bubble formation at submerged orifices," *Chemical Engineering Science*, vol. 50, no. 19, pp. 3009–3024, Oct. 1995.

[15] R. B. H. Tan and I. J. Harris, "A model for non-spherical bubble growth at a single orifice," *Chemical Engineering Science*, vol. 41, no. 12, pp. 3175–3182, Jan. 1986.

[16] C. Ellegaard, A. E. Hansen, A. Haaning, K. Hansen, A. Marcussen, T. Bohr, J. L. Hansen, and S. Watanabe, "Creating corners in kitchen sinks," *Nature*, vol. 392, no. 6678, pp. 767–768, Apr. 1998.

[17] J. W. M. Bush, J. M. Aristoff, and A. E. Hosoi, "An experimental investigation of the stability of the circular hydraulic jump," *Journal of Fluid Mechanics*, vol. 558, p. 33, Jul. 2006.

[18] K. C. Catania, "Underwater Sniffing Guides Olfactory Localization in Semiaquatic Mammals," *Annals of the New York Academy of Sciences*, vol. 1170, no. 1, pp. 407–412, Jul. 2009.

[19] Á. Moreno Soto, P. Peñas, G. Lajoinie, D. Lohse, and D. van der Meer, "Ultrasound-enhanced mass transfer during single-bubble diffusive growth," *Physical Review Fluids*, vol. 5, no. 6, p. 063 605, Jun. 2020, Publisher: American Physical Society.

[20] C. D. Ohl, A. Tijink, and A. Prosperetti, "The added mass of an expanding bubble," *Journal of Fluid Mechanics*, vol. 482, pp. 271–290, May 2003.

[21] D. Quéré, M.-J. Azzopardi, and L. Delattre, "Drops at Rest on a Tilted Plane," *Langmuir*, vol. 14, no. 8, pp. 2213–2216, Apr. 1998.

[22] J. Drelich, J. D. Miller, and R. J. Good, "The Effect of Drop (Bubble) Size on Advancing and Receding Contact Angles for Heterogeneous and Rough Solid Surfaces as Observed with Sessile-Drop and Captive-Bubble Techniques," *Journal of Colloid and Interface Science*, vol. 179, no. 1, pp. 37–50, Apr. 1996.

[23] F. J. M. Ruiz-Cabello, M. A. Rodríguez-Valverde, and M. A. Cabrerizo-Vilchez, "Contact Angle Hysteresis on Polymer Surfaces: An Experimental Study," *Journal of Adhesion Science and Technology*, vol. 25, no. 16, pp. 2039–2049, Jan. 2011.

[24] L. Goehring, L. Mahadevan, and S. W. Morris, "Nonequilibrium scale selection mechanism for columnar jointing," *Proceedings of the National Academy of Sciences*, vol. 106, no. 2, pp. 387–392, Jan. 2009.

[25] X. Ma, J. Lowensohn, and J. C. Burton, "Universal Scaling of Polygonal Desiccation Crack Patterns," *Physical Review E*, vol. 99, no. 1, p. 012 802, Jan. 2019, arXiv: 1807.06126.

[26] J. Hall, A. D. Zaffiro, R. B. Marx, P. C. Kefauver, E. R. Krishnan, R. C. Haught, and J. G. Herrmann, "On-line water quality parameters as indicators of distribution system contamination," *Journal (American Water Works Association)*, vol. 99, no. 1, pp. 66–77, 2007.

[27] K. C. Catania, "Olfaction: Underwater 'sniffing' by semi-aquatic mammals," *Nature*, vol. 444, no. 7122, p. 1024, Dec. 2006.

[28] Yu F. Ivlev, M. V. Rutovskaya, and O. S. Luchkina, "The Use of Olfaction by the Russian Desman (Desmana moschata L.) during Underwater Swimming," *Doklady Biological Sciences*, vol. 452, pp. 280–283, Feb. 2013.

[29] B. A. Craven, E. G. Paterson, and G. S. Settles, "The fluid dynamics of canine olfaction: Unique nasal airflow patterns as an explanation of macrosmia," *Journal of The Royal Society Interface*, rsif20090490, Dec. 2009.

[30] J. Davidson and S. Ryu, "High-speed visualization of soap bubble blowing and image-processing-based analysis of pinch-off dynamics," *Journal of Visualization*, vol. 20, no. 1, pp. 53–61, Feb. 2017.

[31] V. V. Berejnov and R. E. Thorne, "Effect of transient pinning on stability of drops sitting on an inclined plane," *Physical Review E*, vol. 75, no. 6, Jun. 2007, arXiv: physics/0609208.

[32] T.-H. Chou, S.-J. Hong, Y.-J. Sheng, and H.-K. Tsao, "Drops Sitting on a Tilted Plate: Receding and Advancing Pinning," *Langmuir*, vol. 28, no. 11, pp. 5158–5166, Mar. 2012.

[33] A. B. D. Cassie and S. Baxter, "Wettability of Porous Surfaces," *Trans. Faraday Soc.*, vol. 46, pp. 546–551, 1944.

[34] S. Kehl and K. Dettner, "Surviving submerged—Setal tracheal gills for gas exchange in adult rheophilic diving beetles," *Journal of Morphology*, vol. 270, no. 11, pp. 1348–1355, Nov. 2009.

[35] M. R. Flynn and J. W. M. Bush, "Underwater breathing: The mechanics of plastron respiration," *Journal of Fluid Mechanics*, vol. 608, pp. 275–296, Aug. 2008.

[36] R. N. Wenzel, "Resistance of solid surfaces to wetting by water," *Industrial and Engineering Chemistry*, vol. 28, pp. 988–994, 1936.

[37] K. C. Catania and J. H. Kaas, "Somatosensory fovea in the star-nosed mole: Behavioral use of the star in relation to innervation patterns and cortical representation," *The Journal of Comparative Neurology*, vol. 387, no. 2, pp. 215–233, Oct. 1997.

[38] T. Maxworthy, "Bubble rise under an inclined plate," *Journal of Fluid Mechanics*, vol. 229, pp. 659–674, Aug. 1991.

[39] R. J. Benzing and J. E. Myers, "Low Frequency Bubble Formation at Horizontal Circular Orifices," *Industrial & Engineering Chemistry*, vol. 47, no. 10, pp. 2087–2090, Oct. 1955.

[40] F. P. Bretherton, "The motion of long bubbles in tubes," *Journal of Fluid Mechanics*, vol. 10, no. 2, pp. 166–188, Mar. 1961.

[41] S. Das, Y. S. Morsi, G. Brooks, J. J. J. Chen, and W. Yang, "Principal characteristics of a bubble formation on a horizontal downward facing surface," *Colloids and Surfaces A: Physicochemical and Engineering Aspects*, vol. 411, pp. 94–104, Oct. 2012.

[42] S. Hartland and R. W. Hartley, *Axisymmetric fluid-liquid interfaces*. Amsterdam: Elsevier Scientific, 1976.

[43] E. R. Guiler, *Marsupials of Tasmania*. The Trustees of the Tasmanian Museum and Art Gallery, 1960, Type: Book; Book/Illustrated; Government publication.

[44] D. T. Gwynne, K. M. O'Neill, and W. L. Rubink, "The Evolutionary Significance of Fusiform Feces: A Predator-Prey Model," *The Worm Runner's Digest*, vol. 20, no. 1, pp. 91–92, 1978.

[45] B. Triggs, *Wombats*, 2nd ed. Australia: CSIRO Publishing, 2009.

[46] J. Woodford, *The Secret Life of Wombats*. Text Publishing, Jan. 2012, Google-Books-ID: fg_KIKj7fXsC, ISBN: 978-1-921834-90-5.

[47] J. French, *The Secret World of Wombats*. Pymble, Sydney NSW, Australia: Harper-Collins Publishers, 2005, ISBN: 978-0-207-20031-1.

[48] P. J. Yang, M. LaMarca, C. Kaminski, D. I. Chu, and D. L. Hu, "Hydrodynamics of defecation," *Soft Matter*, vol. 13, no. 29, pp. 4960–4970, 2017.

[49] T. Takahashi, "Flow Behavior of Digesta and the Absorption of Nutrients in the Gastrointestine," *Journal of Nutritional Science and Vitaminology*, vol. 57, no. 4, pp. 265–273, 2011.

[50] P. S. Barboza, "Digestive Strategies of the Wombats: Feed Intake, Fiber Digestion, and Digesta Passage in Two Grazing Marsupials with Hindgut Fermentation," *Physiological Zoology*, vol. 66, no. 6, pp. 983–999, 1993.

[51] P. Barboza and I. Hume, "Digestive tract morphology and digestion in the wombats (Marsupialia: Vombatidae)," *Journal Of Comparative Physiology B*, vol. 162, no. 6, Sep. 1992.

[52] G. Hounnou, C. Destrieux, J. Desmé, P. Bertrand, and S. Velut, "Anatomical study of the length of the human intestine," *Surgical and Radiologic Anatomy*, vol. 24, no. 5, pp. 290–294, Dec. 2002.

[53] K. Milton and M. W. Demment, "Digestion and Passage Kinetics of Chimpanzees Fed High and Low Fiber Diets and Comparison with Human Data," *The Journal of Nutrition*, vol. 118, no. 9, pp. 1082–1088, Sep. 1988, Publisher: Oxford Academic.

[54] M. Evans, B. Green, and K. Newgrain, "The field energetics and water fluxes of free-living wombats (Marsupialia: Vombatidae)," *Oecologia*, vol. 137, no. 2, pp. 171–180, Oct. 2003.

[55] A. M. Martin, T. A. Fraser, J. A. Lesku, K. Simpson, G. L. Roberts, J. Garvey, A. Polkinghorne, C. P. Burridge, and S. Carver, "The cascading pathogenic consequences of Sarcoptes scabiei infection that manifest in host disease," *Royal Society Open Science*, vol. 5, p. 180 018, 2018.

[56] C. N. Johnson, "The evolutionary ecology of wombats," *Wombats'. (Eds R.T. Wells and P.A. Pridmore*, pp. 34–41, 1998.

[57] R. T. Wells, P. A. Pridmore, and R. Z. S. of South Australia, Eds., *Wombats*. Norton, N.S.W: Surrey Beatty and Sons in association with the Royal Zoological Society of South Australia, 1998, OCLC: 41666093, ISBN: 978-0-949324-81-8.

[58] R. G. Lentle and P. W. M. Janssen, "Physical characteristics of digesta and their influence on flow and mixing in the mammalian intestine: A review," *Journal of Comparative Physiology B*, vol. 178, no. 6, pp. 673–690, Aug. 2008.

[59] S. M. Woolley, R. S. Cottingham, J. Pocock, and C. A. Buckley, "Shear rheological properties of fresh human faeces with different moisture content," *Water SA*, vol. 40, no. 2, pp. 273–276–276, Jan. 2014.

[60] J. W. Bullard and E. J. Garboczi, "Defining shape measures for 3D star-shaped particles: Sphericity, roundness, and dimensions," *Powder Technology*, vol. 249, pp. 241–252, Nov. 2013.

[61] M. Fernandez Guasti, "Analytic geometry of some rectilinear figures," *International Journal of Math Education Science and Technology*, vol. 23, no. 6, pp. 895–901, 1992.

[62] S. K. Sarna, *Colonic Motility: From Bench Side to Bedside*, ser. Integrated Systems Physiology: From Molecule to Function to Disease. San Rafael (CA): Morgan & Claypool Life Sciences, 2010.

[63] D. Xu, A. Varshney, X. Ma, B. Song, M. Riedl, M. Avila, and B. Hof, "Nonlinear hydrodynamic instability and turbulence in pulsatile flow," *Proceedings of the National Academy of Sciences*, vol. 117, no. 21, pp. 11 233–11 239, May 2020, Publisher: National Academy of Sciences Section: Physical Sciences.

[64] M. M. Bandi, T. Tallinen, and L. Mahadevan, "Shock-driven jamming and periodic fracture of particulate rafts," *EPL (Europhysics Letters)*, vol. 96, no. 3, p. 36 008, Nov. 2011.

[65] D. W. Macdonald, "Patterns of Scent Marking with Urine and Faeces Amongst Carnivore Communities," *Symposium of Zoological Society London*, vol. 45, pp. 107–139, 1980.

[66] I. Barja and R. List, "Faecal marking behaviour in ringtails (Bassariscus astutus) during the non-breeding period: Spatial characteristics of latrines and single faeces," *Chemoecology*, vol. 16, no. 4, pp. 219–222, Dec. 2006.

[67] K. Kilshaw, C. Newman, C. Buesching, J. Bunyan, and D. Macdonald, "Coordinated Latrine Use by European Badgers, Meles meles: Potential Consequences for Territory Defense," *Journal of Mammalogy*, vol. 90, no. 5, pp. 1188–1198, Oct. 2009.

[68] C. Marneweck, A. Jürgens, and A. M. Shrader, "The role of middens in white rhino olfactory communication," *Animal Behaviour*, vol. 140, pp. 7–18, Jun. 2018.

[69] C. E. Merte, T. E. Goodwin, and B. A. Schulte, "Male and female developmental differences in chemosensory investigations by African elephants (Loxodonta africana) approaching waterholes," *Behavioral Ecology and Sociobiology*, vol. 64, no. 3, pp. 401–408, Jan. 2010.

[70] L. Pel, K. A. Landman, and E. F. Kaasschieter, "Analytic solution for the non-linear drying problem," *International Journal of Heat and Mass Transfer*, vol. 45, no. 15, pp. 3173–3180, Jul. 2002.

[71] K. A. Grossenbacher and S. M. McDuffie, "Conductive cooling of lava: Columnar joint diameter and stria width as functions of cooling rate and thermal gradient," *Journal of Volcanology and Geothermal Research*, vol. 69, pp. 95–103, 1995.

[72] M.-M. Xu and D.-H. Wang, "Water deprivation up-regulates urine osmolality and renal aquaporin 2 in Mongolian gerbils (Meriones unguiculatus)," *Comparative Biochemistry and Physiology Part A: Molecular & Integrative Physiology*, vol. 194, pp. 37–44, Apr. 2016.

[73] S. Ostrowski, J. B. Williams, P. Mésochina, and H. Sauerwein, "Physiological acclimation of a desert antelope, Arabian oryx (Oryx leucoryx), to long-term food and water restriction," *Journal of Comparative Physiology B*, vol. 176, no. 3, pp. 191–201, Mar. 2006.

[74] S. Yakabi, H. Karasawa, J. Vu, P. M. Germano, K. Koike, K. Yakabi, J. R. Pisegna, and Y. Tache, "Sa1801 Vasoactive Intestinal Peptide (VIP) Knockout (KO) Mice Show Reduced Daily Water Intake, and Body and Fecal Water Content," *Gastroenterology*, vol. 148, no. 4, S–336, Apr. 2015, Publisher: Elsevier.

[75] M. Abe, Y. Miyajima, T. Hara, Y. Wada, M. Funaba, and T. Iriki, "Factors Affecting Water Balance and Fecal Moisture Content in Suckling Calves Given Dry Feed," *Journal of Dairy Science*, vol. 82, no. 9, pp. 1960–1967, Sep. 1999.

[76] A. Tschudin, M. Clauss, D. Codron, A. Liesegang, and J.-M. Hatt, "Water intake in domestic rabbits (Oryctolagus cuniculus) from open dishes and nipple drinkers under different water and feeding regimes," *Journal of Animal Physiology and Animal Nutrition*, vol. 95, no. 4, pp. 499–511, 2011.

[77] D. O. Freudenberger and I. D. Hume, "Effects of water restriction on digestive function in two macropodid marsupials from divergent habitats and the feral goat," *Journal of Comparative Physiology B*, vol. 163, no. 3, pp. 247–257, Jun. 1993.

[78] M. d. L. C. Silva, P. d. G. L. Speridião, R. Marciano, O. M. S. Amâncio, T. B. de Morais, and M. B. de Morais, "Effects of soy beverage and soy-based formula on growth, weight, and fecal moisture: Experimental study in rats," *Jornal de Pediatria*, vol. 91, no. 3, pp. 306–312, May 2015.

[79] D. Jeong, D.-H. Kim, I.-B. Kang, H. Kim, K.-Y. Song, H.-S. Kim, and K.-H. Seo, "Modulation of gut microbiota and increase in fecal water content in mice induced by administration of Lactobacillus kefiranofaciens DN1," *Food & Function*, vol. 8, no. 2, pp. 680–686, 2017, Publisher: Royal Society of Chemistry.

[80] R. C. Hill, C. F. Burrows, G. W. Ellison, M. D. Finke, J. L. Huntington, and J. E. Bauer, "Water content of faeces is higher in the afternoon than in the morning

in morning-fed dogs fed diets containing texturised vegetable protein from soya," *British Journal of Nutrition*, vol. 106, no. S1, S202–S205, Oct. 2011.

[81] J. Zentek, D. Kaufmann, and T. Pietrzak, "Digestibility and Effects on Fecal Quality of Mixed Diets with Various Hydrocolloid and Water Contents in Three Breeds of Dogs," *The Journal of Nutrition*, vol. 132, no. 6, 1679S–1681S, Jun. 2002.

[82] J. Nery, V. Biourge, C. Tournier, V. Leray, L. Martin, H. Dumon, and P. Nguyen, "Influence of dietary protein content and source on fecal quality, electrolyte concentrations, and osmolarity, and digestibility in dogs differing in body size," *Journal of Animal Science*, vol. 88, no. 1, pp. 159–169, Jan. 2010.

[83] K. Houpt and P. Perry, "Effect of Chronic Furosemide on Salt and Water Intake of Ponies," *Journal of Equine Veterinary Science*, vol. 47, pp. 31–35, Dec. 2016.

[84] S. Williams, J. Horner, E. Orton, M. Green, S. McMullen, A. Mobasheri, and S. L. Freeman, "Water intake, faecal output and intestinal motility in horses moved from pasture to a stabled management regime with controlled exercise," *Equine Veterinary Journal*, vol. 47, no. 1, pp. 96–100, 2015.

[85] M. B. Baldo and C. D. Antenucci, "Diet effect on osmoregulation in the subterranean rodent Ctenomys talarum," *Comparative Biochemistry and Physiology Part A: Molecular & Integrative Physiology*, vol. 235, pp. 148–158, Sep. 2019.

[86] D. K. Lee, S. Jang, E. H. Baek, M. J. Kim, K. S. Lee, H. S. Shin, M. J. Chung, J. E. Kim, K. O. Lee, and N. J. Ha, "Lactic acid bacteria affect serum cholesterol levels, harmful fecal enzyme activity, and fecal water content," *Lipids in Health and Disease*, vol. 8, no. 1, p. 21, Jun. 2009.

[87] K. A. Ribbons, M. G. Currie, J. R. Connor, P. T. Manning, P. C. Allen, P. Didier, M. S. Ratterree, D. A. Clark, and M. J. S. Miller, "The Effect of Inhibitors of Inducible Nitric Oxide Synthase on Chronic Colitis in the Rhesus Monkey," *Journal of Pharmacology and Experimental Therapeutics*, vol. 280, no. 2, pp. 1008–1015, Feb. 1997.

[88] Y.-L. Huang, H.-F. Chu, F.-J. Dai, T.-Y. Yu, and C.-F. Chau, "Intestinal Health Benefits of the Water-Soluble Carbohydrate Concentrate of Wild Grape (Vitis thunbergii) in Hamsters," *Journal of Agricultural and Food Chemistry*, vol. 60, no. 19, pp. 4854–4858, May 2012.

[89] S. C. Jun, E. Y. Jung, D. H. Kang, J. M. Kim, U. J. Chang, and H. J. Suh, "Vitamin C increases the fecal fat excretion by chitosan in guinea-pigs, thereby reducing body weight gain," *Phytotherapy Research*, vol. 24, no. 8, pp. 1234–1241, 2010, _eprint: https://onlinelibrary.wiley.com/doi/pdf/10.1002/ptr.2970.

[90] P. F. Woodall, V. J. Wilson, and P. M. Johnson, "Size and moisture content of faecal pellets of small African antelope and Australian macropods," *African Journal of Ecology*, vol. 37, no. 4, pp. 471–474, Dec. 1999.

[91] J. Lorimer and W. Powers, "Manure Management," in *Manure storages: section2*, 122 Davidson Hall, IA: Midwest Plan Service, Iowa State University, 2001, ISBN: 0-89373-080-7.

[92] L. Goehring, "Drying and cracking mechanisms in a starch slurry," *Physical Review E*, vol. 80, no. 3, p. 036 116, Sep. 2009.

[93] M. Clauss, A. Schwarm, S. Ortmann, W. J. Streich, and J. Hummel, "A case of non-scaling in mammalian physiology? Body size, digestive capacity, food intake, and ingesta passage in mammalian herbivores," *Comparative Biochemistry and Physiology Part A: Molecular & Integrative Physiology*, vol. 148, no. 2, pp. 249–265, Oct. 2007.

[94] J. Halfpenny, *Scats and Tracks of the Rocky Mountains: A Field Guide to the Signs of 70 Wildlife Species*. Rowman & Littlefield, Sep. 2015, ISBN: 978-1-4930-2204-5.

[95] M. R. Blake, J. M. Raker, and K. Whelan, "Validity and reliability of the Bristol Stool Form Scale in healthy adults and patients with diarrhoea-predominant irritable bowel syndrome," *Alimentary Pharmacology & Therapeutics*, vol. 44, no. 7, pp. 693–703, 2016.

[96] K. S. Wang, T. Ma, F. Filiz, A. S. Verkman, and J. A. Bastidas, "Colon water transport in transgenic mice lacking aquaporin-4 water channels," *American Journal of Physiology-Gastrointestinal and Liver Physiology*, vol. 279, no. 2, G463–G470, Aug. 2000.

[97] A. C. Romain and J. Nicolas, "Long term stability of metal oxide-based gas sensors for e-nose environmental applications: An overview," *Sensors and Actuators B: Chemical*, Selected Papers from the 13th International Symposium on Olfaction and Electronic Nose, vol. 146, no. 2, pp. 502–506, Apr. 2010.

[98] V. Dobrokhotov, L. Oakes, D. Sowell, A. Larin, J. Hall, A. Kengne, P. Bakharev, G. Corti, T. Cantrell, T. Prakash, J. Williams, and D. N. McIlroy, "Toward the nanospring-based artificial olfactory system for trace-detection of flammable and explosive vapors," *Sensors and Actuators B: Chemical*, vol. 168, pp. 138–148, Jun. 2012.

[99] A. D'Amico, C. Di Natale, R. Paolesse, A. Macagnano, E. Martinelli, G. Pennazza, M. Santonico, M. Bernabei, C. Roscioni, G. Galluccio, R. Bono, E. F. Agrò, and S. Rullo, "Olfactory systems for medical applications," *Sensors and Actuators B:*

Chemical, Proceedings of the Eleventh International Meeting on Chemical Sensors IMCS-11, vol. 130, no. 1, pp. 458–465, Mar. 2008.

[100]   A. K. Miller, M. C. Hensman, S. Hensman, K. Schultz, P. Reid, M. Shore, J. Brown, K. G. Furton, and S. Lee, "African elephants (Loxodonta africana) can detect TNT using olfaction: Implications for biosensor application," *Applied Animal Behaviour Science*, vol. 171, no. Supplement C, pp. 177–183, Oct. 2015.

[101]   J.-N. Cornu, G. Cancel-Tassin, V. Ondet, C. Girardet, and O. Cussenot, "Olfactory Detection of Prostate Cancer by Dogs Sniffing Urine: A Step Forward in Early Diagnosis," *European Urology*, vol. 59, no. 2, pp. 197–201, Feb. 2011.

[102]   S. Marco and A. Gutierrez-Galvez, "Signal and Data Processing for Machine Olfaction and Chemical Sensing: A Review," *IEEE Sensors Journal*, vol. 12, no. 11, pp. 3189–3214, Nov. 2012.

[103]   M. K. Muezzinoglu, A. Vergara, R. Huerta, N. Rulkov, M. I. Rabinovich, A. Selverston, and H. D. I. Abarbanel, "Acceleration of chemo-sensory information processing using transient features," *Sensors and Actuators B: Chemical*, vol. 137, no. 2, pp. 507–512, Apr. 2009.

[104]   A. Ziyatdinov, J. Fonollosa, L. Fernandez, A. Gutierrez-Galvez, S. Marco, and A. Perera, "Bioinspired early detection through gas flow modulation in chemo-sensory systems," *Sensors and Actuators B: Chemical*, vol. 206, pp. 538–547, Jan. 2015.

[105]   B. A. Craven, G. Geurtsen, G. J. Gillen, J. L. Staymates, M. E. Staymates, R. R. Kunz, T.-H. Ong, T. Mendum, and W. A. MacCrehan, "Biomimetic Sniffing Improves the Detection Performance of a 3D Printed Nose of a Dog and a Commercial Trace Vapor Detector," *Scientific Reports*, vol. 6, p. 36 876, Dec. 2016.

[106]   D. W. Wesson, T. N. Donahou, M. O. Johnson, and M. Wachowiak, "Sniffing Behavior of Mice during Performance in Odor-Guided Tasks," *Chemical Senses*, vol. 33, no. 7, pp. 581–596, Sep. 2008.

[107]   J. Xi, X. A. Si, J. Kim, Y. Zhang, R. E. Jacob, S. Kabilan, and R. A. Corley, "Anatomical Details of the Rabbit Nasal Passages and Their Implications in Breathing, Air Conditioning, and Olfaction," *The Anatomical Record*, vol. 299, no. 7, pp. 853–868, Jul. 2016.

[108]   HorseTigra, *The Sniffing Horse - inspired by Maximus cartoon horse*, Feb. 2013.

[109]   65daysofsteve, *Giraffe sniffs video camera*, Nov. 2008.

[110] A. Nejati, N. Kabaliuk, M. C. Jermy, and J. E. Cater, "A deformable template method for describing and averaging the anatomical variation of the human nasal cavity," *BMC Medical Imaging*, vol. 16, p. 55, Oct. 2016.

[111] S. P. Straszek, F. Taagehøj, S. Graff, and O. F. Pedersen, "Acoustic rhinometry in dog and cat compared with a fluid-displacement method and magnetic resonance imaging," *Journal of Applied Physiology*, vol. 95, no. 2, pp. 635–642, Aug. 2003.

[112] A. N. Ranslow, J. P. Richter, T. Neuberger, B. Van Valkenburgh, C. R. Rumple, A. P. Quigley, B. Pang, M. H. Krane, and B. A. Craven, "Reconstruction and Morphometric Analysis of the Nasal Airway of the White-Tailed Deer (Odocoileus virginianus) and Implications Regarding Respiratory and Olfactory Airflow," *The Anatomical Record*, vol. 297, pp. 2138–2147, 2014.

[113] B. A. Craven, T. Neuberger, E. G. Paterson, A. G. Webb, E. M. Josephson, E. E. Morrison, and G. S. Settles, "Reconstruction and Morphometric Analysis of the Nasal Airway of the Dog (Canis familiaris) and Implications Regarding Olfactory Airflow," *The Anatomical Record: Advances in Integrative Anatomy and Evolutionary Biology*, vol. 290, no. 11, pp. 1325–1340, Nov. 2007.

[114] J. V. Verhagen, D. W. Wesson, T. I. Netoff, J. A. White, and M. Wachowiak, "Sniffing controls an adaptive filter of sensory input to the olfactory bulb," *Nature Neuroscience*, vol. 10, no. 5, pp. 631–639, May 2007.

[115] K. Zhao, P. Dalton, G. C. Yang, and P. W. Scherer, "Numerical Modeling of Turbulent and Laminar Airflow and Odorant Transport during Sniffing in the Human and Rat Nose," *Chemical Senses*, vol. 31, pp. 107–118, 2006.

VITA

Alexander Bo Lee is a graduate student at Georgia Tech. He received his bachelor's degree from Harvey Mudd College in Mathematical and Computational Biology. After graduation, he volunteered in the Peace Corps, teaching middle school math and science in Burkina Faso, West Africa. He has spent the last four years at Georgia Tech, studying the geometry of bubbles and feces. His work has been featured by FY Fluid Dynamics and recognized for an Ig Nobel Prize. After his PhD, Bo will pursue certification to become a high school math teacher.